QUANTIFICATION OF THE EFFECT OF HEMODYNAMIC OCCLUSION IN TWO-PHOTON IMAGING

Baba Yogesh[1,2], Matthias Heindorf[1], Rebecca Jordan[3], & Georg B. Keller[1,2,4]

[1]Friedrich Miescher Institute for Biomedical Research, Basel, Switzerland.
[2]Faculty of Natural Sciences, University of Basel, Basel, Switzerland.
[3]Simons Initiative for the Developing Brain, University of Edinburgh, 1 George Square, EH8 9JZ, Edinburgh, UK.
[4]Correspondence to: georg.keller@fmi.ch

ABSTRACT

The last few years have seen an explosion in the number of tools available to measure neuronal activity using fluorescence imaging (Chen et al., 2013; Feng et al., 2019; Jing et al., 2019; Sun et al., 2018; Wan et al., 2021). When performed in vivo, these measurements are invariably contaminated by hemodynamic occlusion artifacts. In widefield calcium imaging, this problem is well recognized. For two-photon imaging, however, the effects of hemodynamic occlusion have only been sparsely characterized. Here we perform a quantification of hemodynamic occlusion effects using measurements of fluorescence changes observed with GFP expression using both widefield and two-photon imaging. We find that in many instances the magnitude of signal changes attributable to hemodynamic occlusion is comparable to that observed with activity sensors. Moreover, we find that hemodynamic occlusion effects were spatially heterogeneous, both over cortical regions and across cortical depth, and exhibited a complex relationship with behavior. Thus, hemodynamic occlusion is an important caveat to consider when analyzing and interpreting not just widefield but also two-photon imaging data.

INTRODUCTION

Optical imaging of neuronal activity and neuromodulator concentration often involves recording the changes in fluorescence intensity of calcium or neuromodulator sensors expressed in neurons. In vivo, the hemodynamic changes in tissue around at the imaging location can modulate light transmission. Changes in blood volume through vasodilation and vasoconstriction as well as hemoglobin oxygenation change the transmission properties of the tissue. The combination of these effects is referred to as hemodynamic

occlusion. Hemodynamic changes can be driven by local neuronal activity, a phenomenon known as neurovascular coupling (Attwell et al., 2010; Iadecola and Nedergaard, 2007) and are known to contribute significantly to activity measurements in techniques like fiber photometry (Zhang et al., 2022) and widefield microscopy (Ma et al., 2016; Waters, 2020). For these techniques, several methods have been proposed to control for the hemodynamic contribution to these activity measurements (Lohani et al., 2022; Valley et al., 2020; Zhang et al., 2022). However, potential effects of hemodynamic signals on neuronal activity measurements acquired using two-photon imaging remain less well characterized. While it has been shown that arteriole dilation decreases fluorescence recorded in immediately underlying neurons, it is still unclear how large these effects are in a behaving animal where both neuronal activity dynamics and blood pressure and flow variance are likely larger than as previously measured under anesthesia (Shen et al., 2012).

Here, we characterized hemodynamic signals in two-photon imaging of mouse cortex during visuomotor behaviors. We expressed an activity independent marker (GFP) in mouse cortical neurons and measured fluorescence changes using two-photon imaging while mice were interacting with a virtual environment. We found changes in GFP fluorescence in response to locomotion and visual stimuli of a magnitude comparable to that measured with common activity sensors like GCaMP and GRAB variants. GFP signals were apparent both in population average responses and at individual neuron level. Moreover, these signals were heterogeneous over dorsal cortex and cortical layers. We compared the size of GFP signals to the calcium responses reported by GCaMP6 sensors, and to the neuromodulator signals reported by the GRAB sensors for dopamine (GRAB-DA1m), serotonin (GRAB-5HT1.0), acetylcholine (GRAB-ACh3.0), and norepinephrine (GRAB-NE1m). We found that a large fraction of the GRAB response to the different neuromodulators was explained by the GFP signal, consistent with an earlier study characterizing this relationship for GRAB-5HT1.0 and GRAB-5HT3.0 (Ocana-Santero et al., 2024). Based on our findings, we speculate that the primary driver of the hemodynamic signals in two-photon imaging is hemodynamic occlusion. If so, then this problem is likely primarily mitigated by using high dynamic range sensors with low baseline fluorescence, and best controlled for using activity independent fluorescence measurements.

57 **RESULTS**

58 To quantify hemodynamic occlusion in two-photon microscopy we imaged GFP in mouse cortex during
59 behavior. We used an AAV vector (AAV2/1-Ef1α-eGFP-WPRE) injected in primary visual cortex (V1) and
60 anterior cingulate cortex (ACC) to express GFP in cortical neurons (**Figure S1**). Given that the Ef1α
61 promoter biases expression to excitatory neurons, we estimate that most (95%) of the GFP-expressing
62 neurons were excitatory (Attinger et al., 2017). We then used a two-photon microscope to record GFP
63 signals while mice explored a virtual tunnel. Mice were head-fixed on a spherical treadmill surrounded by
64 a toroidal screen and exposed to a set of visuomotor conditions known to activate neurons in V1 and ACC
65 (Attinger et al., 2017; Keller et al., 2012; Leinweber et al., 2017; Zmarz and Keller, 2016). First, mice were
66 exposed to a closed loop condition during which running speed was coupled to visual flow speed in a
67 virtual tunnel. Mice were also exposed to an open loop condition, during which locomotion and visual
68 flow in the virtual tunnel were not coupled, to darkness, and to the presentation of full-field drifting
69 gratings. Throughout all experimental conditions, mice were free to locomote on the spherical treadmill
70 and did so voluntarily. Unless stated otherwise, we will use 'response' to refer to the observed change in
71 GFP fluorescence.

72 ***Locomotion onset and visual stimuli resulted in strong changes in GFP population responses***

73 At the onset of locomotion, we found a transient increase in apparent GFP fluorescence in the population
74 response of layer 2/3 (L2/3) neurons in V1 (**Figure 1A**). This increase in fluorescence of approximately 1%
75 $\Delta F/F_0$ was only marginally smaller than the fluorescence changes typically observed at locomotion onset
76 with genetically encoded calcium indicators (approximately 2% $\Delta F/F_0$ for GCaMP6f (Widmer et al., 2022;
77 Yogesh and Keller, 2023), approximately 1.5% $\Delta F/F_0$ for GCaMP3 (Keller et al., 2012), etc.). By contrast,
78 presentation of full-field drifting gratings resulted in a decrease of the GFP population signal (**Figure 1B**).
79 We observed a similar decrease in GFP population signal on the presentation of an optogenetic
80 stimulation light (637 nm, 10mW after the objective) directed at V1 with either the virtual reality turned
81 on or in the dark (**Figure 1C**). This response was likely visually driven as the decrease was twice as strong
82 in dark than when the virtual reality was on, in line with the stimulation light being more visually salient
83 in dark. Visuomotor mismatches (pauses in the visual flow feedback during locomotion), resulted in an
84 average increase of apparent GFP fluorescence (**Figure 1D**). By design, visuomotor mismatch only occurs
85 during times of locomotion. Because apparent GFP fluorescence increases during locomotion, we
86 estimated the increase expected by chance using random triggers during locomotion to compute the 95%

87 confidence interval in **Figures 1D, 1H, and 1L**. GFP responses to mismatch were only briefly outside these
88 95% confidence intervals. Thus, most stimuli tested drive measurable GFP responses at the population
89 level. However, responses in individual neurons varied considerably (**Figure S2**).

90 To test whether stimulus triggered GFP responses depend on imaging depth and cortical area, we
91 repeated these experiments in layer 5 (L5) of V1 and in L2/3 of ACC. In L5, we found that apparent
92 fluorescence changes at locomotion onset were smaller than those observed in L2/3 (**Figure 1E**). As in
93 L2/3, full-field drifting grating stimuli (**Figure 1F**) and optogenetic stimulation light (**Figure 1G**) both
94 resulted in a significant decrease in apparent GFP fluorescence, while visuomotor mismatch responses
95 were only barely above chance (**Figure 1H**). In L2/3 of ACC, locomotion onset resulted in a strong increase
96 of apparent GFP fluorescence (**Figure 1I**), while we found only small grating responses (**Figure 1J**) and a
97 positive response to optogenetic stimulation light (**Figure 1K**). We again found no evidence of visuomotor
98 mismatch responses (**Figure 1L**). Thus, apparent GFP fluorescence changes can vary both as a function of
99 recording depth and cortical area.

100 The observation that average population responses of GFP and calcium indicators are similar does not
101 mean that the dynamic range of individual neurons is similar. When comparing the distribution of peak
102 $\Delta F/F_0$ responses, it is evident that peak responses are much larger for calcium indicators (**Figures 2A and**
103 **2B**). This is still the case when comparing trial averaged responses (**Figures 2C-2E**), but the difference
104 between GFP and calcium indicator response distributions is smaller, in particular for locomotion onsets
105 (**Figure 2C**). The main driver for this effect is likely the highly variable stimulus triggered calcium responses
106 of many neurons.

107 ***Individual neurons showed significant GFP responses to different stimuli***

108 Next, we tested whether GFP signals are strong enough to result in significant responses when looking at
109 individual neurons. Raw GFP traces exhibited fluctuations reminiscent of calcium responses but tended to
110 be of lower peak amplitude (**Figure 2A**). It is possible that small, correlated changes in GFP signal, when
111 averaged over the population, result in a significant response indistinguishable from calcium signals
112 reported with GCaMP but are negligible at the level of individual neurons. Thus, we quantified the fraction
113 of neurons that are significantly responsive to different stimuli. GFP expression levels were high enough
114 for all neurons in our dataset such that peak $\Delta F/F_0$ response amplitudes were independent of baseline F_0
115 (**Figure S4**). Commensurate with the population averages (**Figure 1**), we found a surprisingly large fraction

116 of neurons in V1, in both L2/3 (**Figure 3A**) and L5 (**Figure 3B**) responsive to locomotion onset and grating
117 stimuli. In both locations, the fraction of neurons responsive to visuomotor mismatch was not different
118 from chance. In ACC L2/3 (**Figure 3C**), a significant fraction of GFP labelled neurons was responsive to
119 locomotion onset, while the fraction of neurons responsive to gratings and visuomotor mismatch was not
120 different from chance. In all cases, the fraction of neurons responsive as measured with GFP was similar
121 to the fraction of neurons responsive as measured with GCaMP (**Figures 3D-3F**). Thus, even at the single
122 neuron level, hemodynamic influence on GFP remains sizable.

123 ***Changes in GFP fluorescence correlated with blood vessel dilation***

124 One possible source of changes in GFP fluorescence is brain motion. However, we only find detectable
125 brain motion during locomotion onsets and not the other stimuli (**Figure S5**), and even during locomotion
126 onsets the movements are comparably small and follow different kinematics than the GFP signals. Finally,
127 brain motion artefacts should on average decrease fluorescence, as they will move the cell out of the ROI.
128 Thus, we speculated that the dominant change in GFP fluorescence is driven by hemodynamic occlusion
129 (see **Discussion** for alternative possibilities). Blood absorbs light. This absorption changes both as a
130 function of blood volume and blood oxygenation. Thus, the blood vessels on the cortical surface that are
131 between the GFP labeled neurons and the objective of the microscope act to variably occlude the
132 fluorescence measurement. As they constrict, dilate, or change oxygenation, they influence the
133 transmission of both excitation and emission light similar to how an LCD (liquid crystal display) functions.
134 One testable prediction of this hypothesis is that the cross section of blood vessels visible in a given field
135 of view should correlate inversely with the apparent GFP fluorescence of surrounding cells. This makes
136 the simplifying assumption that the cross section of surface blood vessels, which likely have the strongest
137 contribution to occlusion, correlates with that of blood vessels in the imaging plane. To quantify the
138 correlation between blood vessel cross section and apparent GFP fluorescence, we first estimated the
139 cross section of selected blood vessels in the imaging plane (**Figures 4A-4C**). Blood vessels in V1 dilated
140 systematically, for example upon light stimulation (**Figures 4A1 and 4B1**), and contracted, for example on
141 locomotion onset in ACC (**Figure 4C1**). The estimation of blood vessel cross section worked well for high
142 contrast boundaries but failed in many instances of low contrast boundaries due to noise in the boundary
143 estimates in single imaging frames. A proxy for blood vessel cross section that does not rely on
144 thresholding is the average fluorescence of a region of interest of fixed size and fully contained within the
145 blood vessel (**Figures 4A2, 4B2, 4C2**). The intuition here is that there should be no fluorescence inside the

146 blood vessel. Thus, fluorescence measured inside the blood vessel must come from the fact that the point
147 spread function of the microscope extends to regions outside of the blood vessel. As the blood vessel
148 contracts (or dilates) more (or less) of GFP in the tissue around the blood vessel will move into the point
149 spread function. Comparing both metrics to the average apparent GFP fluorescence changes of the
150 surrounding cells (**Figures 4A3, 4B3, 4C3**), we found that both blood vessel area and fluorescence explain
151 over 80% of the variance of apparent GFP fluorescence changes (**Figures 4A4, 4B4, 4C4**) in these example
152 data. Here, variance explained is defined as the squared linear correlation coefficient between blood
153 vessel area and fluorescence. Quantifying this for all data, we found that the fraction of variance explained
154 was 50% or higher for most event triggered averages (**Figure 4D**) as well as across the entire recording
155 duration (**Figures 4E and S6**). The variance explained tended to be lower in ACC than in V1; we suspect
156 that this is caused by the superior sagittal sinus contributing more strongly to hemodynamic occlusion in
157 ACC, and that the diameters of local blood vessels are less well correlated with that of this large blood
158 vessel. Consistent with vasoconstriction causing the increase of signal on locomotion onset, we sometimes
159 find patterns of fluorescence changes that look like blood vessels that pass immediately above the imaging
160 plan (**Figures S7A and S7B**). More typical however, is a broad increase that likely is driven by hemodynamic
161 changes in blood vessels closer to the surface of the brain (**Figures S7C and S7D**).

162 ***GFP responses were visuomotor context sensitive and could not be explained by a linear combination of***
163 ***responses to constituent stimuli***

164 Next, we investigated how stereotypical GFP responses are across different visuomotor conditions and
165 cortical regions, and whether GFP responses can be explained by a linear combination of a locomotion
166 driven component and a visually driven component. We found that in V1 L2/3, locomotion onset
167 responses were similar in closed loop and open loop, but different in the dark (**Figure 5A**). During a closed
168 loop locomotion onset, there is concurrent onset of visual flow with the locomotion onset. During open
169 loop and dark locomotion onsets there is no concurrent onset of visual flow, and they only differ in the
170 average visual input. The similarity between open and closed loop running onsets could be explained by
171 a dominant locomotion related signal and a negligible visual onset response. If so, the smaller GFP
172 responses in dark locomotion would need to be the consequence of the lower average visual input. This
173 demonstrates that GFP responses, similar to neuronal calcium responses, can be non-linear combinations
174 of component responses. This is perhaps not surprising, assuming local blood flow is primarily related to
175 local neuronal activity. In L5 of V1, locomotion onset responses in open loop and dark conditions were

comparable, while those in closed loop conditions had a delayed transient dip (**Figure 5B**). Thus, hemodynamic responses can exhibit a strong depth dependence. In ACC L2/3 neurons all three types of locomotion onsets resulted in increases of apparent fluorescence (**Figure 5C**). Thus, hemodynamic responses are difficult to predict from component signals (**Figure S3**), and do not generalize across depth or cortical areas. Finally, while there appears to be some correspondence to local neuronal activity in that locomotion onsets are more strongly modulated by visual context in V1 than in ACC, it is not immediately obvious how the GFP signals relate to responses measured with calcium indicators.

Locomotion increased correlation in GFP signals

Another metric frequently used in the analysis of two-photon data are correlation-based analyses. Locomotion, for example, has been shown to decorrelate the activity of excitatory neurons in cortex (Aydın et al., 2018; Dadarlat and Stryker, 2017; Erisken et al., 2014; Yogesh and Keller, 2023). Given the sizable fraction of neurons significantly responsive to locomotion, we speculated that correlations between neurons likely are influenced by hemodynamic responses. We tested this by quantifying the effect of locomotion on the pairwise correlations of GFP signals between individual neurons. We found that pairwise correlations were systematically increased during locomotion (**Figure 6**). This was true for neurons in V1 L2/3 (**Figure 6A**), V1 L5 (**Figure 6B**), and ACC L2/3 (**Figure 6C**). Thus, hemodynamic responses can have a strong influence on pairwise correlations, and in the case of locomotion, this effect is opposite to that observed with calcium indicators (Aydın et al., 2018; Dadarlat and Stryker, 2017; Erisken et al., 2014; Yogesh and Keller, 2023). This is consistent with the interpretation that hemodynamic changes on locomotion occur at a larger spatial scale than changes in neuronal activity patterns and thus tend to increase correlations between neurons.

GFP responses in widefield imaging were similar in magnitude to those in two-photon imaging

In widefield calcium imaging, hemodynamic responses are better characterized and widely recognized as a confounding problem (Allen et al., 2017; Ma et al., 2016; Valley et al., 2020). To directly contrast hemodynamic widefield signals with those observed in two-photon imaging, we repeated our experiments by performing widefield imaging of GFP responses. We expressed GFP pan-neuronally across dorsal cortex using either a retro-orbital injection of AAV-PHP.eB-EF1α-eGFP, or transgenic mice that express GFP under a *c-fos* promoter (**Table S2**). As with two-photon imaging (**Figure 1**), and consistent with previous work (Allen et al., 2017; Valley et al., 2020), we found strong GFP responses across dorsal

205 cortex (**Figure 7**). Locomotion and grating onsets resulted in GFP responses in both V1 (**Figures 7A and**
206 **7B**) and ACC (**Figures 7D and 7E**). During visuomotor mismatch, we found no significant response in either
207 of these regions (**Figures 7C and 7F**). All these responses were greatly attenuated or absent when we
208 imaged the cortex without expressing a fluorescent indicator (**Figure S8**), arguing in favor of hemodynamic
209 occlusion of fluorescence from the genetically expressed indicators as the underlying cause for most of
210 these responses in the GFP signal.

211 ***GRAB sensors in cortex displayed similar responses to those recorded in GFP imaging***

212 Finally, we compared the magnitude of hemodynamic responses to those recorded with the relatively low
213 dynamic range GRAB sensors using both two-photon and widefield imaging. For this we used the GRAB-
214 DA1m dopamine sensor (Sun et al., 2018), the GRAB-5HT1.0 serotonin sensor (Wan et al., 2021), the
215 GRAB-ACh3.0 acetylcholine sensor (Jing et al., 2019), and the GRAB-NE1m(Feng et al., 2019)
216 norepinephrine sensor (Feng et al., 2019). We first imaged GRAB-DA1m, GRAB-5HT1.0, and GRAB-ACh3.0
217 using two-photon imaging in L2/3 of V1. To estimate hemodynamic responses from GRAB sensors, we
218 compared responses of regions of interest (ROI) selected in neuropil and those selected in blood vessels
219 (**Figures 8A, 8E and 8I**). We reasoned that the signal in neuropil regions is a combination of a true GRAB
220 signal and hemodynamic occlusion, while the signal in a ROI selected inside of a blood vessel should be
221 dominated by the blood vessel diameter. We found that the GRAB-DA1m response to locomotion and
222 full-field grating onsets (**Figure 8B and 8C**) was similar to GFP responses in V1 L2/3 (**Figure 1**). There were
223 responses to locomotion and grating onset in the GRAB-DA1m signal (**Figure 8B and 8C**). In both cases
224 neuropil and blood vessel ROI responses were similar. Also, similar to the GFP responses, we found no
225 evidence of a response to visuomotor mismatch in the GRAB-DA1m signal (**Figure 8D**). We observed
226 similar responses when imaging GRAB-5HT1.0 in V1 (**Figures 8F-8H**). However, these responses were
227 smaller in amplitude, likely driven by the overall dimmer fluorescence of the GRAB-5HT1.0 sensor. Thus,
228 it is likely that both GRAB-DA1m and GRAB-5HT1.0 responses recorded with two-photon imaging are
229 dominated by hemodynamic occlusion.

230 A response that was distinct from GFP, GRAB-DA1m, and GRAB-5HT1.0 signals was the response in GRAB-
231 ACh3.0 on locomotion onset (**Figure 8J**). Here we found a prominent increase in GRAB-ACh3.0 signal that
232 was three-fold higher than either the GFP signal or the GRAB-ACh3.0 signals measured in blood vessel
233 ROIs. This makes it more likely that the observed fluorescence changes are driven by a mixture of
234 hemodynamic occlusion and GRAB-ACh3.0 responses. The GRAB-ACh3.0 response to grating onset (**Figure**

235 **8K**), however, was similar to GFP responses. And again, we found no response to visuomotor mismatch in
236 GRAB-ACh3.0 (**Figure 8L**). To test whether the absence of response differences between GRAB-DA1m,
237 GRAB-5HT1.0 and GFP signals was simply a result of imaging in V1, where both dopamine and serotonin
238 release is weaker than in frontal areas of cortex (Berger et al., 1991; Hamada et al., 2023), we repeated
239 these experiments in ACC. Also here, we found no evidence of GRAB responses that could not be explained
240 by hemodynamic occlusion (**Figure S9**). A strong influence of hemodynamic signals was also apparent in
241 widefield imaging of GRAB-NE1m. We found that the widefield GRAB-NE1m responses (**Figure 9**) were
242 similar to GFP responses (**Figure 7**). Thus, in certain cases of low dynamic range sensors, one can readily
243 measure responses, but these are not always easily distinguished from those driven by hemodynamic
244 occlusion.

245 **DISCUSSION**

246 Our data demonstrate that in vivo two-photon fluorescence imaging during behavior is subject to
247 relatively large and fast changes in measured fluorescence independent of any sensor typically used to
248 measure functional calcium, voltage, or peptide changes. The surprising finding to us, was not that these
249 changes are observed, but rather how large they are on a population average compared to fluorescence
250 changes measured with functional sensors. There are several possible sources of these fluorescence
251 changes:

252 **Brain movement artifacts.** Many body movements result in the movement of the brain relative to the
253 skull. In our experience, locomotion onset as well chewing and licking (or other movements that involve
254 the masseter muscles) are the strongest drivers of such movements. Use of a cranial window prevents
255 much of the movement in the axis perpendicular to the window (which typically is the optical axis). To
256 mitigate this problem, we discard any experimental preparation with visible z-motion, and correct x/y
257 motion using a full-frame registration algorithm. For locomotion onsets, brain movement kinematics are
258 different in shape than the GFP responses we observe, and in the case of visual stimulation, we find no
259 evidence of stimulus driven brain movements (**Figure S5**). Finally, given that the regions of interest used
260 to quantify fluorescence changes are selected based on a mean position of the neuron, movement away
261 from the mean position should result in an average decrease in observed fluorescence. Thus, while there
262 certainly are brain movement related artifacts that can strongly influence two-photon measurements if
263 not properly mitigated, these artifacts cannot explain visual stimulation induced fluorescence changes,

264 and likely only explain the initial, fast decrease of fluorescence observed in a subset of neurons at
265 locomotion onset (**Figure S2**).

266 **Stimulation light contamination.** Light from the visual display system can leak into the optical pathway of
267 the two-photon microscope. This results in stimulus locked changes in fluorescence that can occur both
268 for visual stimulation, but also for closed loop locomotion onsets, as locomotion triggers an onset of visual
269 flow. This can be partially mitigated by physically shielding the imaging site from stimulation light.
270 However complete shielding is difficult (e.g. some of the stimulation light likely travels through the eye to
271 the brain and into the microscope – the fact that light quite efficiently travels this route is what has
272 enabled convenient eye tracking in two photon imaging as the stimulation light from the two-photon laser
273 illuminates the pupil from the inside). In two photon imaging this problem can however be almost
274 completely solved by synchronizing all light sources in the experimental setup to the dead times of the
275 microscope (e.g. the turnaround times of the resonant scanner) (Leinweber et al., 2014), as we have also
276 done here. Finally, stimulation light contamination exhibits essentially immediate onset and offset kinetics
277 and is relatively simple to recognize. Thus, we are confident that stimulation light contamination does not
278 significantly contribute to the effects we describe here.

279 **GFP's sensitivity to pH changes.** GFP changes its fluorescence with changes in pH (Kneen et al., 1998).
280 And intracellular pH systematically changes with neuronal activity. While the relationship between
281 neuronal activity and intracellular pH is complex and not fully understood, increases in neuronal activity
282 tend to result in decreases of intracellular pH. Thus, the activity driven pH change should decrease GFP
283 fluorescence. What we find, however, in many cases is a positive correlation between neuronal activity
284 and GFP fluorescence. More importantly, however, intracellular pH changes driven by neuronal activity
285 are on the order of 0.1 around a resting pH somewhere between 7 and 8 (Chesler, 2003; Raimondo et al.,
286 2013). While GFP is indeed sensitive to pH, this is primarily the case for pH values below 6. The
287 fluorescence changes above a pH of 7 are comparably small, and likely negligible when the changes are in
288 the range of 0.1 (Dos Santos et al., 2020; Kneen et al., 1998). Thus, we don't think the pH sensitivity of
289 GFP substantially contributes to the effects we observe.

290 **Hemodynamic tissue deformation.** A second type of movement artifact is produced by local tissue
291 deformations caused by blood vessel diameter changes. Cells in close proximity to a blood vessel are
292 displaced when blood vessels dilate and contract. These effects are primarily visible in cells in the
293 immediate vicinity (a few cell body diameters) of blood vessels. As with brain movement driven artefacts,

294 the net effect of such tissue deformations is to displace the cell away from the region of interest used to
295 measure fluorescence and hence result they tend to result in apparent fluorescence decreases on
296 average. These effects certainly also contribute to the signals we report but given the observed increase
297 in fluorescence on running onset, the effect of hemodynamic tissue deformation are likely smaller
298 compared to that of occlusion. Moreover, these effects are primarily visible when there is a high
299 fluorescence inside a ROI and low fluorescence immediately surrounding it (e.g. as is the case when
300 expressing GFP or GCaMP). When expressing GRAB sensors, labelling is much more homogeneous, and
301 there are no distinct contrast changes at the edges of ROIs. Thus, the fact that the hemodynamic driven
302 signals look very similar when labelling is primarily confined to somata (**Figure 1**), compared to using GRAB
303 sensors (**Figure 8**), is consistent with our interpretation that hemodynamic tissue deformations are not
304 the primary driver of the signals we report.

305 **Hemodynamic occlusion.** Blood absorbs stimulation and emission light. As a function of volume and
306 composition of blood, light absorption can change dynamically. Changes in neuronal activity in the cortex
307 are associated with hemodynamic changes through neurovascular coupling (Ruff et al., 2024) that are
308 layer specific (Mächler et al., 2021). Cells directly under arterioles have been shown to be occluded by
309 changes in arteriole diameter (Shen et al., 2012). In brain structures like cortex that have a relatively dense
310 blood vessel network on the surface, this problem is augmented as any blood vessel within the imaging
311 light cone between the surface of the brain and the recorded cell will contribute to the occlusion. Using
312 an objective with a numerical aperture of 1, this is a light cone with a half angle of approximately 45
313 degrees. Thus, when e.g. imaging a neuron at a depth of 500 µm, all surface vessels in circle around
314 location of the neuron of 1 mm diameter will contribute to the occlusion. Even ignoring occlusion
315 contributions that arise from changes to the composition of blood (e.g. oxygenation changes), the changes
316 driven by blood vessel cross section changes are likely sufficient to explain the effect sizes we observe.
317 Thus, we conclude that hemodynamic occlusion is the primary contributor to the effects we observe.
318 Some of the other factors discussed above certainly also contribute to the effects we describe, and there
319 may yet be other influences we have not thought of yet. Importantly however, all these factors similarly
320 would contribute to signals measured with functional indicators.

321 **How to mitigate the problem.** There are likely two approaches: use a second imaging channel for
322 concurrent isosbestic illumination of the sensor or estimate the hemodynamic contribution in a separate
323 set of experiments using GFP. For the calcium indicator GCaMP, isosbestic imaging has been shown to

work in widefield imaging (Allen et al., 2017; Couto et al., 2021). However, imaging at the isosbestic wavelength concurrently with the functional measurement would require a second tunable two-photon light source. In the case of fiber photometry (Zhang et al., 2022) and widefield imaging (Ma et al., 2016; Scott et al., 2018; Valley et al., 2020) hemodynamic influence is well documented, and there are correction methods published (Allen et al., 2017; Ma et al., 2016). But even here methods based on isosbestic illumination can be difficult to implement accurately, either because light sources used for isosbestic illumination are not tunable or not available at the exact wavelength necessary, or when using LEDs, have emission spectra are too broad. One could consider trying a model based approach to estimate hemodynamic occlusion effects based on GFP measurements, as can be done for widefield imaging (Valley et al., 2020). However, because hemodynamic occlusion changes across the cortical surface and depth, separate GFP calibrations are likely necessary for different regions and layers imaged. Finally, a simple but laborious approach is to repeat key experiments using GFP to test how much of the functional effects can be explained by non-functional effects. While arguably more than a decade too late (Keller et al., 2012), this is what our aim was here.

Finally, given that hemodynamic changes are likely driven by neuronal activity through neurovascular coupling (Ruff et al., 2024), which can be highly specific to cortical layer (Mächler et al., 2021), these signals could be a useful proxy to estimate neuronal activity. Assuming one would identify a neuronal cell-type with activity that correlates well with local hemodynamic changes, blood vessel diameter measurements could be used as a relatively simple secondary measurement in functional two-photon imaging.

344 **METHODS**

345 Key Resources Table

Reagent type (species) or resource	Designation	Source or reference	Identifier	Additional information
Strain, strain background (adeno-associated virus)	AAV2/1-Ef1α-eGFP-WPRE (10^{12} GC/ml)	FMI vector core	vector.fmi.ch	
Strain, strain background (adeno-associated virus)	AAV2/1-Ef1α-GCaMP6f-WPRE (10^{11}-10^{14} GC/ml)	FMI vector core	vector.fmi.ch	
Strain, strain background (adeno-associated virus)	AAV2/9-hSyn-GRAB-DA1m (10^{12} GC/ml)	FMI vector core	vector.fmi.ch	
Strain, strain background (adeno-associated virus)	AAV2/9-hSyn-GRAB-5HT1.0 (10^{13} GC/ml)	FMI vector core	vector.fmi.ch	
Strain, strain background (adeno-associated virus)	AAV2/9-hSyn-GRAB-ACh3.0 (10^{13} GC/ml)	FMI vector core	vector.fmi.ch	
Strain, strain background (adeno-associated virus)	AAV-PHP.eB-EF1α-eGFP (10^{13} GC/ml)	FMI vector core	vector.fmi.ch	
Strain, strain background (adeno-associated virus)	AAV-PHP.eB-hSyn-GRAB-NE1m (10^{13} GC/ml)	FMI vector core	vector.fmi.ch	
Chemical compound, drug	Fentanyl citrate	Actavis	CAS 990-73-8	Anesthetic compound
Chemical compound, drug	Midazolam (Dormicum)	Roche	CAS 59467-96-8	Anesthetic compound
Chemical compound, drug	Medetomidine (Domitor)	Orion Pharma	CAS 86347-14-0	Anesthetic compound
Chemical compound, drug	Ropivacaine	Presenius Kabi	CAS 132112-35-7	Analgesic compound
Chemical compound, drug	Lidocaine	Bichsel	CAS 137-58-6	Analgesic compound
Chemical compound, drug	Buprenorphine	Reckitt Benckiser Healthcare	CAS 52485-79-7	Analgesic compound
Chemical compound, drug	Humigel	Virbac	-	Ophthalmic gel
Chemical compound, drug	Flumazenil (Anexate)	Roche	CAS 78755-81-4	Anesthetic antagonist
Chemical compound, drug	Atipamezole (Antisedan)	Orion Pharma	CAS 104054-27-5	Anesthetic antagonist
Chemical compound, drug	Metacam	Boehringer Ingelheim	CAS 71125-39-8	Analgesic compound
Chemical compound, drug	N-Butyl-2-cyanoacrylate	Braun	CAS 6606-65-1	Histoacryl
Chemical compound, drug	Dental cement (Paladur)	Heraeus Kulzer	CAS 9066-86-8	

Genetic reagent *Mus musculus*	*C57BL/6*	Charles River	-	
Genetic reagent *Mus musculus*	*B6J.129S6-Chat$^{tm2(Cre)Lowl}$/MwarJ* Alias used here: ChAT-IRES-Cre	Jackson Laboratories	RRID:IMSR_JAX:028861	Cre expression in cholinergic neurons
Genetic reagent *Mus musculus*	*B6J.FVB(Cg)-Tg(Tlx3-cre)PL56Gsat/Mmucd* Alias used here: Tlx3-Cre	MMRRC	RRID:MMRRC_041158-UCD	Cre expression in a subset of L5 neurons
Genetic reagent *Mus musculus*	*B6.Cg-Tg(Fos/EGFP)1-3Brth/J* Alias used here: fosGFP	Jackson Laboratories	RRID:IMSR_JAX:014135	Cre expression in a subset of cortical neurons
Software, algorithm	MATLAB (2023b)	The MathWorks	RRID:SCR_001622	Data analysis
Software, algorithm	LabVIEW	National Instruments	RRID:SCR_014325	Hardware control
Software, algorithm	Two-photon acquisition software	Keller laboratory	sourceforge.net/p/iris-scanning/	Data acquisition
Software, algorithm	Image data processing software	Keller laboratory	sourceforge.net/p/iris-scanning/calliope	Data processing
Software, algorithm	Python	python.org	RRID:SCR_008394	Virtual reality
Software, algorithm	Panda3D	panda3d.org	N/A	Virtual reality
Other	Virtual reality and two-photon setup	(Leinweber et al., 2014, 2017)	DOI: 10.3791/50885, 10.1016/j.neuron.2017.08.036	Hardware setup
Other	OBIS 673 nm LX	Coherent	Cat#1187194	Optogenetic stimulation laser
Other	LED	Prizmatix	UHP-T-595	Sham stimulation
Other	Titanium headplate	FMI/ETHZ workshop	N/A	Mice head-fixation
Other	Dental drill	Meisinger	N/A	For craniotomy

Mice. We used a total of 35 C57BL/6 mice, 4 fosGFP mice, 6 Tlx3-Cre mice, and 23 ChAT-IRES-Cre mice. Both male and female mice, 6 - 16 weeks old at the start of the experiment, were used. See **Table S2** for details of mouse inclusion for different figures. Between experiments, mice were group-housed in a vivarium (light/dark cycle: 12/12 hours). All animal procedures were approved by and carried out in accordance with the guidelines laid by the Veterinary Department of the Canton of Basel-Stadt, Switzerland.

353 **Surgery.** For all surgical procedures, mice were anesthetized with a mixture of fentanyl (0.05 mg/kg;
354 Actavis), midazolam (5.0 mg/kg; Dormicum, Roche), and medetomidine (0.5 mg/kg; Domitor, Orion)
355 injected intraperitoneally. Analgesics were applied perioperatively (2% lidocaine gel, meloxicam 5 mg/kg)
356 and postoperatively (buprenorphine 0.1 mg/kg, meloxicam 5 mg/kg). Eyes were covered with ophthalmic
357 gel (Virbac Schweiz AG). Depending on the experiment, we either implanted a cranial window to perform
358 two-photon imaging or used crystal skull (or clear skull preparation in case of GRAB-NE1m imaging) for
359 widefield imaging. Cranial windows were implanted over V1 and ACC as previously described (Keller et al.,
360 2012; Leinweber et al., 2014). Briefly, using a dental drill, a 4 mm craniotomy was made over the right V1,
361 centered 2.5 mm lateral and 0.5 mm anterior to lambda. A second craniotomy was made over right ACC,
362 centered at midline, 0.5 mm anterior to bregma. After injection of an AAV vector carrying the reporter
363 (see **Table S2** for details of virus), the exposed cortex was sealed with a 3 mm or 4 mm circular glass
364 coverslip and glued in place using gel superglue (Ultra Gel, Pattex). The remaining exposed surface of the
365 skull was covered with Histoacryl (B. Braun), and a titanium head bar was fixed to the skull using dental
366 cement (Paladur, Heraeus Kulzer). For widefield experiments, we injected an AAV vector with PHP.eB
367 capsid retro-orbitally (6 µl per eye of at least 10^{13} GC/ml) to drive expression throughout cortex, or imaged
368 GFP expressed in a fosGFP mice, or imaged without any fluorophore. For crystal skull surgery, we surgically
369 removed the skull plate overlying the dorsal cortex and superglued a crystal skull coverslip over the
370 craniotomy. Prior to removing the skull plate overlying dorsal cortex, the location of bregma relative to
371 other landmarks on the skull was recorded. For clear skull preparation, the skull was cleared with a three-
372 component polymer (C&B Metabond, Parkell), and the crystal skull coverslip was directly attached to the
373 skull. An epifluorescence image was taken to mark reference points on cortical surface. As with 4mm
374 cranial window implantation, a titanium head bar was fixed to the skull using dental cement. After surgery,
375 anesthesia was antagonized by a mixture of flumazenil (0.5 mg/kg; Anexate, Roche) and atipamezole (2.5
376 mg/kg; Antisedan, Orion Pharma) injected intraperitoneally. Imaging commenced earliest 2 weeks after
377 head bar implantation or 3 weeks after retro-orbital AAV injection.

378 **Virtual reality environment.** The virtual reality setup is based on the design of Dombeck and colleagues
379 (Dombeck et al., 2007). Briefly, mice were head-fixed and free to run on an air-supported spherical
380 treadmill. The rotation of the ball was restricted around the vertical axis with a pin. The virtual reality
381 environment was projected onto a toroidal screen covering approximately 240 degrees horizontally and
382 100 degrees vertically of the mouse's visual field, using a projector (Samsung SP-F10M) synchronized to
383 the resonant scanner of the two-photon microscope such that visual stimulation occurs at the turnaround

384 time of the resonant scanner, during which any photon reaching the PMT is discarded, thereby allowing
385 for near-simultaneous stimulation-artifact-free imaging. The virtual environment consisted of an infinite
386 corridor with walls patterned with vertical sinusoidal gratings with a spatial frequency of approximately
387 0.04 cycles per degree (Leinweber et al., 2014). In closed loop sessions, the locomotion of the mouse was
388 coupled to movement along a virtual tunnel. In open loop sessions, we uncoupled the two and replayed
389 the visual flow from a preceding closed loop session. In grating sessions, we presented full-field drifting
390 gratings (0°, 45°, 90°, 270°, moving in either direction) in a pseudo-random sequence. Grating stimuli were
391 presented for between 1 s and 8 s depending on the experiment. In the inter-stimulus interval, mice were
392 shown a gray screen with average luminance matched to that of the grating stimuli. For optogenetic light
393 stimulation, we used 1 s pulses (10 mW after the objective) of a red laser (637 nm) directed at visual cortex
394 through a cranial window.

395 **Two-photon imaging.** Two-photon calcium imaging was performed using custom-built microscopes
396 (Leinweber et al. 2014). The illumination source was a tunable femtosecond laser (Insight, Spectra Physics
397 or Chameleon, Coherent) tuned to 930 nm. Emission light was band-pass filtered using a 525/50 filter for
398 GCaMP and a 607/70 filter for tdTomato/mCherry (Semrock) and detected using a GaAsP photomultiplier
399 (H7422, Hamamatsu). Photomultiplier signals were amplified (DHPCA-100, Femto), digitized (NI5772,
400 National Instruments) at 800 MHz, and band-pass filtered at 80 MHz using a digital Fourier-transform filter
401 implemented in custom-written software on an FPGA (NI5772, National Instruments). The scanning
402 system of the microscopes was based on a 12 kHz resonant scanner (Cambridge Technology). Images were
403 acquired at a resolution of 750 x 400 pixels (60 Hz frame rate), and a piezo-electric linear actuator (P-726,
404 Physik Instrumente) was used to move the objective (Nikon 16x, 0.8 NA) in steps of 15 µm between frames
405 to acquire images at 4 different depths. This resulted in an effective frame rate of 15 Hz. We imaged layer
406 2/3 at a depth of 100-250 µm, and layer 5 at a depth of 400-600 µm. The field of view was 375 µm x 300
407 µm.

408 **Widefield imaging.** Widefield imaging experiments were conducted on a custom-build macroscope with
409 commercially available objectives mounted face-to-face (Nikon 85 mm/f1.8 sample side, Nikon 50
410 mm/f1.4 sensor side). A 470 nm LED (Thorlabs) powered by a custom-build LED driver was used to excite
411 GFP through an excitation filter (SP490, Thorlabs) reflected off a dichroic mirror (LP490, Thorlabs) placed
412 parfocal to the objectives. The fluorescence was collected through a 525/50 emission filter on a sCMOS
413 camera (PCO edge 4.2). LED illumination was adjusted with a collimator (Thorlabs SM2F32-A) to

414 homogenously illuminate cortical surface through the cranial window. An Arduino board (Arduino Mega
415 2560) was used to synchronize LED onset with frame trigger signal of the camera. The duty cycle of the
416 470 nm LED was 90%. Images were acquired at 50 Hz or 100 Hz effective frame rate. Raw images were
417 cropped on the sensor and data was stored to disk with custom-written LabVIEW (National Instruments)
418 software, resulting in an effective pixel size of 60 μm^2 at a resolution of 1108 pixels x 1220 pixels (1.35
419 MP).

420 **Extraction of neuronal and GRAB activity.** Two-photon calcium imaging data were processed as
421 previously described (Keller et al., 2012) and all data analysis was done in MATLAB (MathWorks). Briefly,
422 raw images were full-frame registered to correct for lateral brain motion. All data with visible z-motion
423 were excluded. Neurons were manually selected based on mean and maximum fluorescence images. For
424 GRAB imaging, neuropil and blood vessels were manually selected. Raw fluorescence traces were
425 corrected for slow drift in fluorescence using an 8th-percentile filtering with a 66 s (or 1000 frames)
426 window (Dombeck et al., 2007). $\Delta F/F_0$ traces were calculated as mean fluorescence in a selected region
427 of every imaging frame, subtracted and normalized by the overall median fluorescence. No neuropil
428 subtraction was done. All two-photon calcium and GRAB imaging data was acquired at 15 Hz.

429 For widefield macroscope imaging, raw movie data was manually registered across days by aligning
430 subsequent mean projections of the data to the first recorded image sequence. ROIs were placed relative
431 to readily identifiable anatomical landmarks that had been previously noted during cranial window
432 surgery (see above). This resulted in the selection of six 20 pixels x 20 pixels ROIs per hemisphere. Of those
433 ROIs, we calculated the activity as the $\Delta F/F_0$, wherein F_0 was the median fluorescence of the recording
434 (approximately 30 000 frames in a 5 min recording). $\Delta F/F_0$ was corrected for slow fluorescence drift caused
435 by thermal brightening of the LED using 8th percentile filtering with a 62.5 s moving window similar to
436 what's described above for two-photon imaging.

437 **Extraction of blood vessel area.** To measure the area of blood vessels, we manually identified rectangular
438 ROIs encompassing the blood vessels and a surrounding margin of neuropil, as depicted in **Figures 4A and**
439 **4B**. We generated a trigger-averaged video from these ROIs by averaging the video across all instances of
440 optogenetic stimulation under dark condition. We applied a threshold set at the 0.5^{th} percentile of all pixel
441 intensities in the video to binarize each frame. Subsequently, frame-wise we fitted an ellipse to the
442 connected pixels that fell below this threshold, isolating the blood vessel. The area of this ellipse served
443 as an estimate of the blood vessel area.

Data analysis. All data analysis was done using custom scripts written in MATLAB (MathWorks). To quantify the average population response traces, we first calculated the average event-triggered fluorescence trace for each ROI. The responses of all ROIs were then averaged and baseline-subtracted.

Locomotion onset was defined as running speed crossing a threshold of 0.25 cm/s for at least 1 s, while having been below the threshold during the preceding 1 s. The same criteria were used to define visual flow onsets in the open loop condition using visual flow speed. Visuomotor mismatch responses were probed by presenting brief 1 s full-field visual flow halts in the closed loop condition. For a visuomotor mismatch event to be included in analysis, mice had to be locomoting uninterrupted above threshold (0.25 cm/s) from -0.5 s to +1 s after the event onset. Additionally, for a ROI to be included for analysis of the response to a particular event, it had to have at least 3 onsets to the event. The GFP response was baseline subtracted using a -0.5 s to 0 s window relative to onset. The same was -1 s to -0.5 s in case of locomotion onset to account for preparatory activity.

In **Figures 2C-2E**, to compare GFP and GCaMP responses, we trial averaged the response of individual neurons and used the mean response over a time-window of 0 s to +2.0 s relative to locomotion or visuomotor mismatch onset, with a baseline subtraction window of -1 s to -0.5 s. For grating responses, we used the mean of the trial averaged response over +0.5 s to +3.0 s relative to stimulus onset, with a baseline subtraction window of -0.5 s to 0 s.

In **Figure 3**, for each neuron, we averaged the response from +0.5 s to +1.5 s relative to onset for individual locomotion onset and visuomotor mismatch trials and tested if the mean of this distribution is significantly different from 0 using a t-test with a chance threshold of 5% . In a similar analysis, the response window for grating responsive neurons was set at +0.5 s to +2.5 s to account for the 2 s long grating stimuli.

In **Figure 4**, the blood vessel diameter and the average GFP signal from both blood vessel ROIs and neuropil ROIs were smoothed with a 0.5 s moving average and the variance explained was computed on the -2.0 s to +6.0 s window relative to stimulus onset with a linear model (i.e. R^2, where R is the linear correlation coefficient between the two signals). In **Figure 4D**, data points were drawn as outliers if they were larger than 75th percentile + 1.5*(75th percentile - 25th percentile) or smaller than 25th percentile - 1.5*(75th percentile - 25th percentile) of the distribution and were omitted from the figure.

In **Figures 7** and **S8**, due to insufficient triggers, we relaxed the locomotion threshold for mismatch to 0.12 cm/s, and in **Figure S8**, we relaxed the sitting window before locomotion onset to -0.5 s to 0 s.

Statistical Analysis. All statistical information for the tests performed in the manuscript is provided in **Table S1**. Unless stated otherwise, the shading indicates the error in mean estimation to within 1 standard deviation. For analysis where the experimental unit was neurons (or ROIs), we used hierarchical bootstrap (Saravanan et al., 2020) for statistical testing due to the nested nature (neurons (or ROIs) and mice) of the data. Briefly, we trial averaged the data for the respective event per neuron (or ROI), and first resampled the data (with replacement) at the level of imaging sites, and then, from the selected sites, resampled for neurons. We then computed the mean of this bootstrap sample and repeated this N times to generate a bootstrap distribution of the mean estimate. For all statistical testing the number of bootstrap samples (N) was 10 000, for plotting bootstrap mean and standard error response curves it was 1000. The bootstrap standard error is the 68% confidence interval (1 SD, 15.8th percentile to 84.2nd percentile) in the bootstrap distribution of the mean.

484 **SUPPLEMENTARY INFORMATION**

485 **Table S1. Statistical information on all analysis.**

Figure panel	Value compared	Test	P-value	N (ROIs)	N (Sites)	N (Mice)
1A	Locomotion onset response in V1 L2/3	-	-	2647	6	6
1B	Grating onset response in V1 L2/3	-	-	2647	6	6
1C	Visual response to opto stim light in V1 L2/3	-	-	2647	6	6
1D	Visuomotor mismatch response in V1 L2/3	-	-	2218	5	5
1E	Locomotion onset response in V1 L5	-	-	1463	6	6
1F	Grating onset response in V1 L5	-	-	1463	6	6
1G	Visual response to opto stim light in V1 L5	-	-	1463	6	6
1H	Visuomotor mismatch response in V1 L5	-	-	947	4	4
1I	Locomotion onset response in ACC L2/3	-	-	2417	6	6
1J	Grating onset response in ACC L2/3	-	-	2417	6	6
1K	Visual response to opto stim light in ACC L2/3	-	-	2417	6	6
1L	Visuomotor mismatch response in ACC L2/3	-	-	2417	6	6
2B-2E	GCaMP6f *vs* GFP	-	-	15 103, 6527	51, 18	15, 6
3A	Fraction of L2/3 neurons in V1 classified responsive to locomotion onsets based on GFP signals	Hierarchical bootstrap	$<10^{-4}$	2647	6	6
	Fraction of L2/3 neurons in V1 classified responsive to grating onsets based on GFP signals	Hierarchical bootstrap	$<10^{-4}$	2647	6	6
	Fraction of L2/3 neurons in V1 classified responsive to mismatch onsets based on GFP signals	Hierarchical bootstrap	0.34	2218	5	5
	Fraction of L2/3 neurons in V1 classified responsive to locomotion onsets *vs* grating onset based on GFP signals	Hierarchical bootstrap	$<10^{-4}$	2647, 2647	6,6	6,6
	Fraction of L2/3 neurons in V1 classified responsive to grating onsets *vs* mismatch onset based on GFP signals	Hierarchical bootstrap	$<10^{-4}$	2647, 2218	6,5	6,5
	Fraction of L2/3 neurons in V1 classified responsive to locomotion onsets *vs* mismatch onset based on GFP signals	Hierarchical bootstrap	$<10^{-4}$	2647, 2218	6,5	6,5
3B	Fraction of L5 neurons in V1 classified responsive to locomotion onsets based on GFP signals	Hierarchical bootstrap	$<10^{-4}$	1463	6	6
	Fraction of L5 neurons in V1 classified responsive to grating onsets based on GFP signals	Hierarchical bootstrap	$<10^{-4}$	1463	6	6
	Fraction of L5 neurons in V1 classified responsive to mismatch onsets based on GFP signals	Hierarchical bootstrap	0.09	947	4	4

	Fraction of L5 neurons in V1 classified responsive to locomotion onsets *vs* grating onset based on GFP signals	Hierarchical bootstrap	0.08	1463, 1463	6,6	6,6
	Fraction of L5 neurons in V1 classified responsive to grating onsets *vs* mismatch onset based on GFP signals	Hierarchical bootstrap	$<10^{-4}$	1463, 947	6,4	6,4
	Fraction of L5 neurons in V1 classified responsive to locomotion onsets *vs* mismatch onset based on GFP signals	Hierarchical bootstrap	$<10^{-4}$	1463, 947	6,4	6,4
3C	Fraction of L2/3 neurons in ACC classified responsive to locomotion onsets based on GFP signals	Hierarchical bootstrap	$<10^{-4}$	2417	6	6
	Fraction of L2/3 neurons in ACC classified responsive to grating onsets based on GFP signals	Hierarchical bootstrap	0.18	2417	6	6
	Fraction of L2/3 neurons in ACC classified responsive to mismatch onsets based on GFP signals	Hierarchical bootstrap	0.34	2417	6	6
	Fraction of L2/3 neurons in ACC classified responsive to locomotion onsets *vs* grating onset based on GFP signals	Hierarchical bootstrap	$<10^{-4}$	2417, 2417	6,6	6,6
	Fraction of L2/3 neurons in ACC classified responsive to grating onsets *vs* mismatch onset based on GFP signals	Hierarchical bootstrap	0.57	2417, 2417	6,6	6,6
	Fraction of L2/3 neurons in ACC classified responsive to locomotion onsets *vs* mismatch onset based on GFP signals	Hierarchical bootstrap	$<10^{-4}$	2417, 2417	6,6	6,6
3D	Fraction of L2/3 neurons in V1 classified responsive to locomotion onsets based on GCaMP6f signals	Hierarchical bootstrap	$<10^{-4}$	7971	25	15
	Fraction of L2/3 neurons in V1 classified responsive to grating onsets based on GCaMP6f signals	Hierarchical bootstrap	$<10^{-4}$	7971	25	15
	Fraction of L2/3 neurons in V1 classified responsive to mismatch onsets based on GCaMP6f signals	Hierarchical bootstrap	$<10^{-4}$	7653	24	15
	Fraction of L2/3 neurons in V1 classified responsive to locomotion onsets *vs* grating onset based on GCaMP6f signals	Hierarchical bootstrap	0.01	7971, 7971	25, 25	15, 15
	Fraction of L2/3 neurons in V1 classified responsive to grating onsets *vs* mismatch onset based on GCaMP6f signals	Hierarchical bootstrap	$<10^{-4}$	7971, 7653	25, 24	15, 15
	Fraction of L2/3 neurons in V1 classified responsive to locomotion onsets *vs* mismatch onset based on GCaMP6f signals	Hierarchical bootstrap	$<10^{-4}$	7971, 7653	25, 24	15, 15
3E	Fraction of L5 neurons in V1 classified responsive to locomotion onsets based on GCaMP6f signals	Hierarchical bootstrap	$<10^{-4}$	7132	26	14
	Fraction of L5 neurons in V1 classified responsive to grating onsets based on GCaMP6f signals	Hierarchical bootstrap	$<10^{-4}$	7132	26	14
	Fraction of L5 neurons in V1 classified responsive to mismatch onsets based on GCaMP6f signals	Hierarchical bootstrap	$<10^{-3}$	6812	25	13

	Fraction of L5 neurons in V1 classified responsive to locomotion onsets *vs* grating onset based on GCaMP6f signals	Hierarchical bootstrap	0.19	7132, 7132	26, 26	14, 14
	Fraction of L5 neurons in V1 classified responsive to grating onsets *vs* mismatch onset based on GCaMP6f signals	Hierarchical bootstrap	$<10^{-4}$	7132, 6812	26, 25	14, 13
	Fraction of L5 neurons in V1 classified responsive to locomotion onsets *vs* mismatch onset based on GCaMP6f signals	Hierarchical bootstrap	$<10^{-4}$	7132, 6812	26, 25	14, 13
3F	Fraction of L2/3 neurons in ACC classified responsive to locomotion onsets based on GCaMP signals	Hierarchical bootstrap	$<10^{-4}$	2207	12	7
	Fraction of L2/3 neurons in ACC classified responsive to mismatch onsets based on GCaMP signals	Hierarchical bootstrap	$<10^{-4}$	2207	12	7
	Fraction of L2/3 neurons in ACC classified responsive to locomotion onsets *vs* mismatch onset based on GCaMP signals	Hierarchical bootstrap	$<10^{-4}$	2207, 2207	12,12	7,7
4D-4E	Variance explained in V1 L2/3 neuron GFP signal	-	-	2647	6	6
4D-4E	Variance explained in V1 L5 neuron GFP signal	-	-	1463	6	6
4D-4E	Variance explained in ACC L2/3 neuron GFP signal	-	-	2417	6	6
5A	Locomotion onset response under different conditions in V1 L2/3	-	-	2647	6	6
5B	Locomotion onset response under different conditions in V1 L5	-	-	1463	6	6
5C	Locomotion onset response under different conditions in ACC L2/3	-	-	2417	6	6
6A	Pairwise correlation in GFP signal in V1 L2/3 neurons, stationary *vs* locomoting	Hierarchical bootstrap	$<10^{-3}$	2647	6	6
6B	Pairwise correlation in GFP signal in V1 L5 neurons, stationary *vs* locomoting	Hierarchical bootstrap	$<10^{-4}$	1276	6	6
6C	Pairwise correlation in GFP signal in ACC L2/3 neurons, stationary *vs* locomoting	Hierarchical bootstrap	$<10^{-4}$	2417	6	6
7A	Locomotion onset response in V1	-	-	48	24	11
7B	Grating onset response in V1	-	-	52	26	12
7C	Visuomotor mismatch response in V1	-	-	48	24	11
7D	Locomotion onset response in ACC	-	-	48	24	11
7E	Grating onset response in ACC	-	-	52	26	12
7F	Visuomotor mismatch response in ACC	-	-	48	24	11
8B	Locomotion onset response in GRAB-DA1m in V1 – neuropil and blood vessel ROI response	-	-	168, 34	7, 5	7, 5
8C	Grating onset response in GRAB-DA1m in V1 – neuropil and blood vessel ROI response	-	-	168, 34	7, 5	7, 5

8D	Visuomotor mismatch response in GRAB-DA1m in V1 – neuropil and blood vessel ROI response	-	-	124, 20	5, 3	5, 3
8F	Locomotion onset response in GRAB-5HT1.0 in V1 – neuropil and blood vessel ROI response	-	-	220, 113	10, 10	9, 9
8G	Grating onset response in GRAB-5HT1.0 in V1 – neuropil and blood vessel ROI response	-	-	205, 101	9, 9	9, 9
8H	Visuomotor mismatch response in GRAB-5HT1.0 in V1 – neuropil and blood vessel ROI response	-	-	193, 101	9, 9	8, 8
8J	Locomotion onset response in GRAB-ACh3.0 in V1 – neuropil and blood vessel ROI response	-	-	178, 118	8,8	8,8
8K	Grating onset response in GRAB-ACh3.0 in V1 – neuropil and blood vessel ROI response	-	-	178, 118	8,8	8,8
8L	Visuomotor mismatch response in GRAB-ACh3.0 in V1 – neuropil and blood vessel ROI response	-	-	178, 118	8,8	8,8
9A	Locomotion onset response in GRAB-NE1m in V1	-	-	64	32	5
9B	Grating onset response in GRAB-NE1m in V1	-	-	12	6	5
9C	Visuomotor mismatch response in GRAB-NE1m in V1	-	-	18	9	5
9D	Locomotion onset response in GRAB-NE1m in ACC	-	-	64	32	5
9E	Grating onset response in GRAB-NE1m in ACC	-	-	12	6	5
9F	Visuomotor mismatch response in GRAB-NE1m in ACC	-	-	18	9	5
S2A	Locomotion onset response in V1 L2/3	-	-	2647	6	6
	Grating onset response in V1 L2/3	-	-	2647	6	6
	Visual response to opto stim light in dark in V1 L2/3	-	-	2647	6	6
	Visual response to opto stim light in VR in V1 L2/3	-	-	2647	6	6
	Visuomotor mismatch response in V1 L2/3	-	-	2218	5	5
S2B	Locomotion onset response in V1 L5	-	-	1463	6	6
	Grating onset response in V1 L5	-	-	1463	6	6
	Visual response to opto stim light in dark in V1 L5	-	-	1463	6	6
	Visual response to opto stim light in VR in V1 L5	-	-	1463	6	6
	Visuomotor mismatch response in V1 L5	-	-	947	4	4
S2C	Locomotion onset response in ACC L2/3	-	-	2417	6	6
	Grating onset response in ACC L2/3	-	-	2417	6	6
	Visual response to opto stim light in dark in ACC L2/3	-	-	2417	6	6
	Visual response to opto stim light in VR in ACC L2/3	-	-	2417	6	6
	Visuomotor mismatch response in ACC L2/3	-	-	2417	6	6
S3A	Visual flow onset response with GFP in V1 L2/3	-	-	2647	6	6
S3B	Locomotion onset response in dark with GFP in V1 L2/3	-	-	2647	6	6
S3C	Visual flow onset response in closed loop with GFP in V1 L2/3	-	-	2647	6	6

S4	Average peak GFP response for low vs intermediate GFP expression level	Hierarchical bootstrap	0.88	7076, 6477	17, 15	6, 6
	Average peak GFP response for intermediate vs high GFP expression level	Hierarchical bootstrap	0.36	6477, 4857	15, 10	6, 6
	Average peak GFP response for low vs high GFP expression level	Hierarchical bootstrap	0.85	7076, 4857	17, 10	6, 6
S5A	Brain velocity on locomotion onset	-	-	-	18	6
S5B	Brain velocity on grating onset	-	-	-	18	6
S5C	Brain velocity on opto stim light onset in dark	-	-	-	18	6
S5D	Brain velocity on opto stim light onset in VR	-	-	-	18	6
S8A	Locomotion onset response with widefield and no fluorophore in V1	-	-	24	12	6
S8B	Grating onset response with widefield and no fluorophore in V1	-	-	24	12	6
S8C	Visuomotor mismatch response with widefield and no fluorophore in V1	-	-	16	8	4
S8D	Locomotion onset response with widefield and no fluorophore in ACC	-	-	24	12	6
S8E	Grating onset response with widefield and no fluorophore in ACC	-	-	24	12	6
S8F	Visuomotor mismatch response with widefield and no fluorophore in ACC	-	-	16	8	4
S9A	Locomotion onset response in GRAB-DA1m in V1 – neuropil and blood vessel ROI response	-	-	122, 61	7, 7	7, 7
S9B	Grating onset response in GRAB- DA1m in V1 – neuropil and blood vessel ROI response	-	-	122, 61	7, 7	7, 7
S9C	Visuomotor mismatch response in GRAB- DA1m in V1 – neuropil and blood vessel ROI response	-	-	80, 50	5, 5	5, 5
S9D	Locomotion onset response in GRAB-5HT1.0 in ACC – neuropil and blood vessel ROI response	-	-	123, 79	7, 7	6, 6
S9E	Grating onset response in GRAB-5HT1.0 in ACC – neuropil and blood vessel ROI response	-	-	109, 69	6, 6	6, 6
S9F	Visuomotor mismatch response in GRAB-5HT1.0 in ACC – neuropil and blood vessel ROI response	-	-	91, 56	5, 5	5, 5

487 **Table S2. Number of mice in different experimental groups.**

Genotype	Virus	Site of injection	Nbr. Mice	Nbr. ROIs	Figures
C57BL/6	AAV2/1-Ef1α-eGFP-WPRE	Primary visual cortex – L2/3	6	3072	Figures 1, 2, 3A, 4, 5, 6, S1, S2, S3, S4, S5, S7
C57BL/6	AAV2/1-Ef1α-eGFP-WPRE	Primary visual cortex – L5	6	1710	Figures 1, 2, 3B, 4, 5, 6, S1, S2, S3, S4, S5, S6, S7
C57BL/6	AAV2/1-Ef1α-eGFP-WPRE	Anterior cingulate cortex – L2/3	6	2739	Figures 1, 2, 3C, 4, 5, 6, S1, S2, S3, S4, S5, S6, S7
ChAT-IRES-Cre	AAV2/1-Ef1α-GCaMP6f-WPRE	Primary visual cortex – L2/3 and L5	15	15 103	Figures 2, 3D, 3E
C57BL/6	AAV-PHP.eB-EF1α-eGFP	Retro-orbital	8	32	Figure 7
fosGFP	-	-	4	20	Figure 7
Tlx3-Cre	-	-	6	24	Figure S8
ChAT-IRES-Cre	AAV2/9-hSyn-GRAB-ACh3.0	Primary visual cortex	8	609	Figure 8
C57BL/6	AAV2/9-hSyn-GRAB-DA1m	Anterior cingulate cortex	7	183	Figures 8, S9
		Primary visual cortex	7	202	
C57BL/6	AAV2/9-hSyn-GRAB-5HT1.0	Anterior cingulate cortex	9	202	Figures 8, S9
		Primary visual cortex	6	333	
C57BL/6	AAV-PHP.eB-hSyn-GRAB-NE1m	Retro-orbital	5	156	Figure 9

488

FIGURES

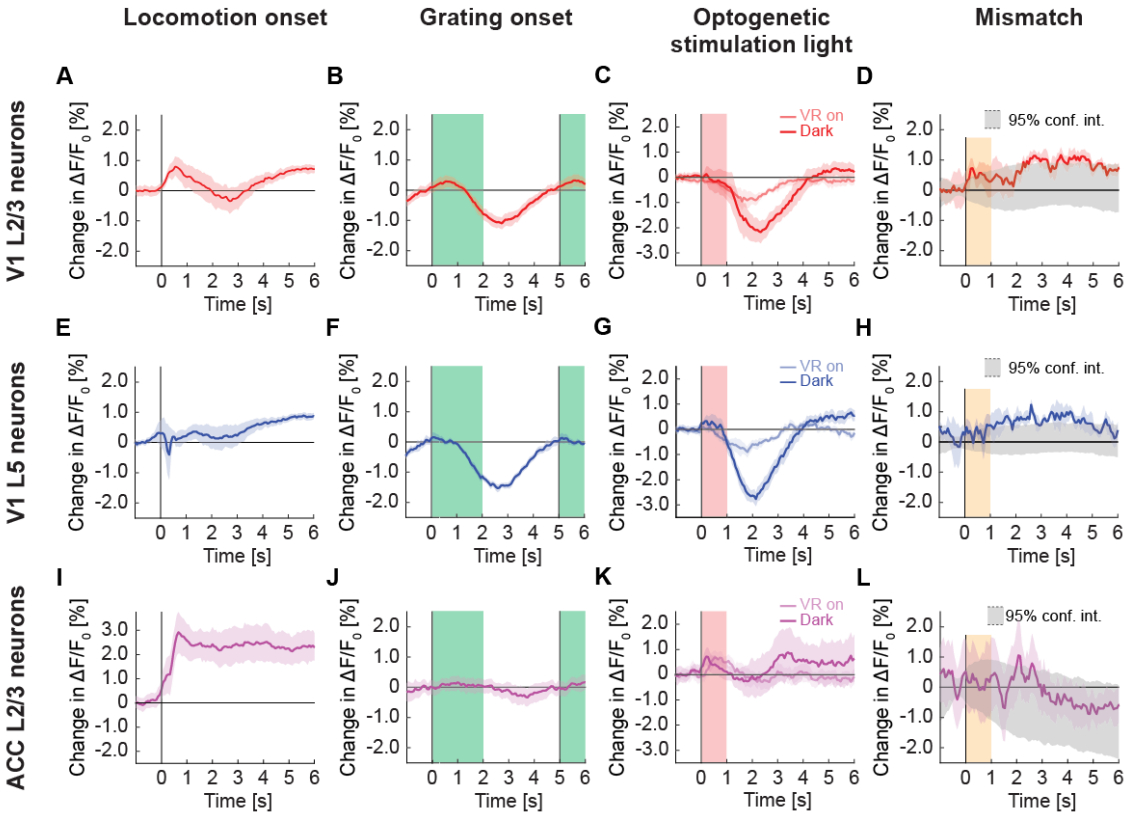

Figure 1. GFP responses in two-photon imaging of neurons in V1 and ACC.

(**A**) Average change in apparent GFP fluorescence in L2/3 neurons in V1 on locomotion onset. Mean (solid lines) and the bootstrap standard error (shading) are calculated as hierarchical bootstrap estimate for each time bin.

(**B**) As in **A**, but for grating onsets in L2/3 neurons in V1. Green shading marks the duration of the gratings.

(**C**) As in **A**, but for responses to optogenetic stimulation light in L2/3 neurons in V1, with VR on (light red) or in dark (dark red). Pink shading marks the duration of the light stimulus.

(**D**) As in **A**, but for visuomotor mismatch in L2/3 neurons in V1. Orange shading marks the duration of visuomotor mismatch. As mismatch events are defined to occur during times of locomotion, and locomotion itself drives GFP responses, we would expect to find an increase in these signals by chance at mismatch. To correct for this, we quantified the distribution of signal amplitude on random triggers during locomotion (95% confidence interval, gray shading).

(**E**) As in **A**, but for L5 neurons in V1.

(**F**) As in **B**, but for L5 neurons in V1.

(**G**) As in **C**, but for L5 neurons in V1.

(**H**) As in **D**, but for L5 neurons in V1.

(**I**) As in **A**, but for L2/3 neurons in ACC.

(**J**) As in **B**, but for L2/3 neurons in ACC.

(**K**) As in **C**, but for L2/3 neurons in ACC.

(**L**) As in **D**, but for L2/3 neurons in ACC.

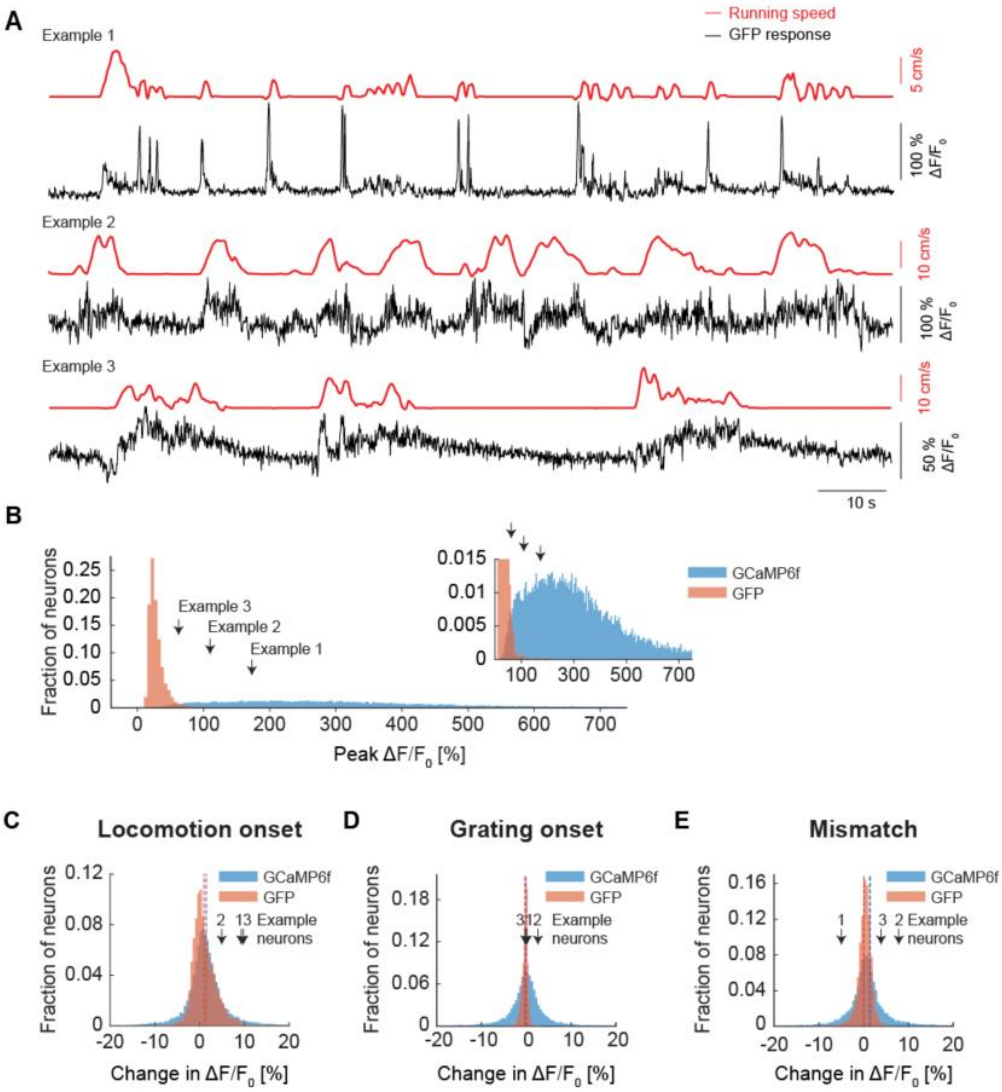

Figure 2. Peak responses of GCaMP6f were larger than those observed with GFP.

(**A**) Example GFP response traces (black) of three neurons with corresponding running speed traces (red).

(**B**) Peak responses of GCaMP6f (blue) were typically an order of magnitude larger than those observed with GFP (orange). Inset is a zoomed-in version of the same data.

(**C**) Histogram of trial averaged responses on locomotion onset measured with two-photon imaging of calcium indicator (blue) and GFP (orange). Dotted lines indicate the mean response of the distribution of locomotion onset response in calcium indicator (blue) and GFP (orange).

(**D**) As in **C**, but for grating onset.

(**E**) As in **C**, but for visuomotor mismatch.

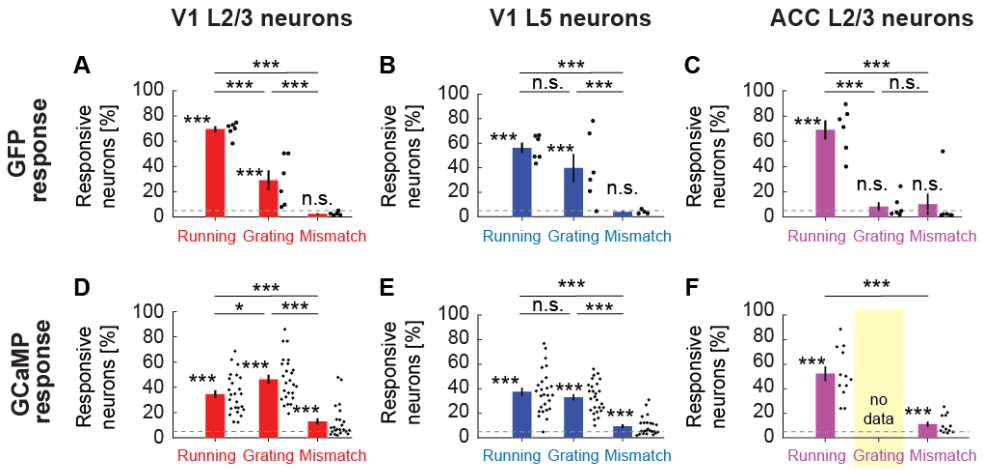

521

522 **Figure 3. Fraction of neurons with significant GFP responses to different stimuli.**

523 (**A**) The fraction of GFP expressing V1 L2/3 neurons responsive to locomotion, full-field grating, and
524 visuomotor mismatch onset, quantified for all imaging sites. Each dot is an imaging site, jittered along the
525 x-axis to make them visible. Whiskers mark the SEM. Dashed line indicates chance levels ($p = 0.05$). n.s.:
526 not significant; *: $p < 0.05$; **: $p < 0.01$; ***: $p < 0.001$; see **Table S1** for all statistical information.

527 (**B**) As in **A**, but for V1 L5 neurons.

528 (**C**) As in **A**, but for ACC L2/3 neurons.

529 (**D**) As in **A**, but for V1 L2/3 neurons expressing GCaMP6f.

530 (**E**) As in **A**, but for V1 L5 neurons expressing GCaMP6f.

531 (**F**) As in **A**, but for ACC L2/3 neurons expressing a GCaMP variant (data are from experiments using
532 GCaMP3, GCaMP5, GCaMP6s, and GCaMP6f). Note, we have no grating presentation for this population.

533

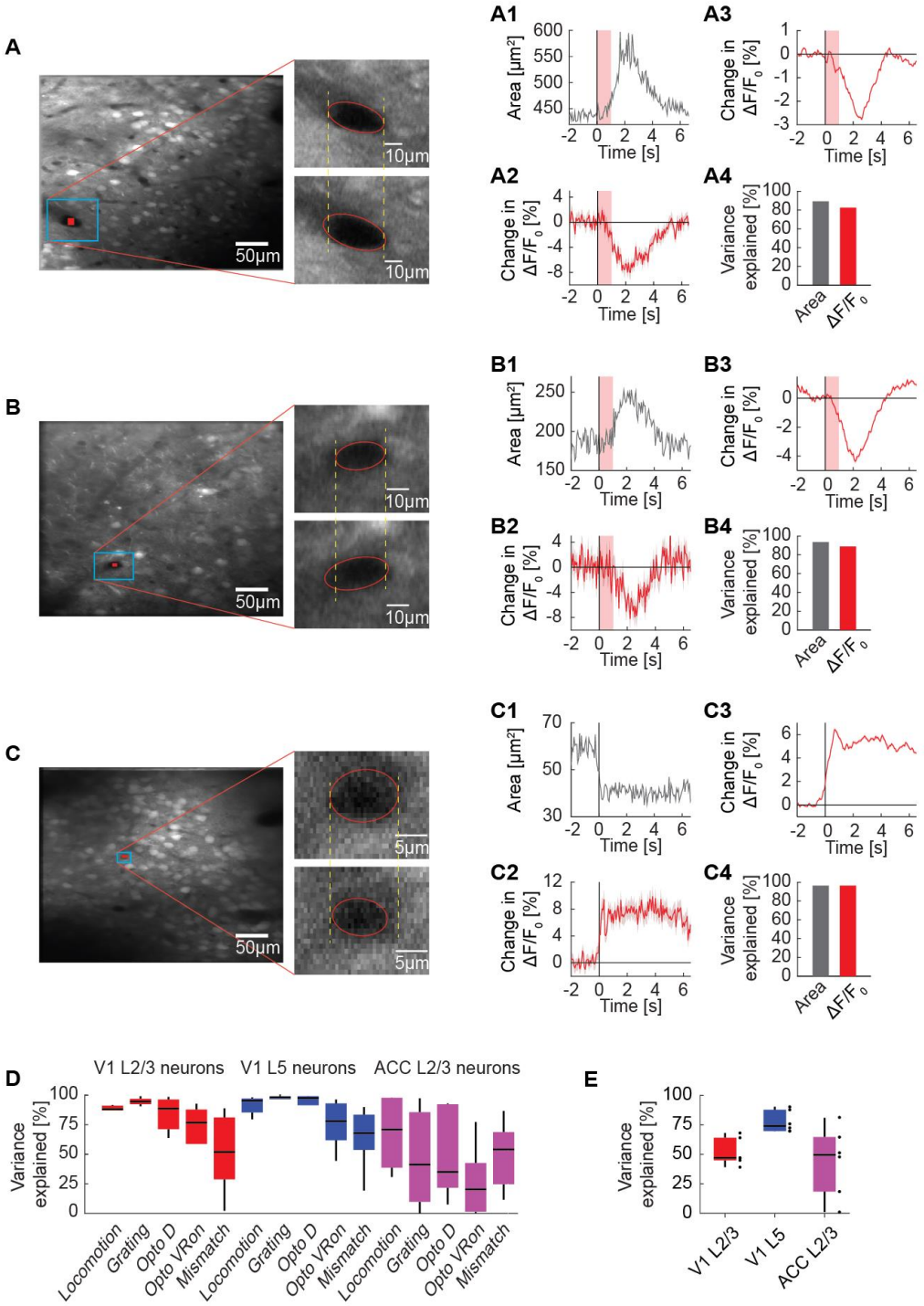

Figure 4. Correlation between blood vessel area and GFP responses.

(**A**) Example average fluorescence image from an imaging site in L2/3 of V1 under a two-photon microscope. The fluorescence signal is averaged over 22 trials of optogenetic stimulation light directed at

538 V1 while the mouse was in the dark. Shown on the right is an example blood vessel before (upper panel)
539 and after (lower panel) stimulation.

540 (**A1**) Average area of the example blood vessel shown in **A** (in blue box) on light stimulation. The area of
541 the indicated blood vessel is extracted from the trial averaged two-photon image. Shading in pink
542 indicates the optogenetic light presentation.

543 (**A2**) Average change in GFP signal from a ROI positioned within the blood vessel (shown in **A** in red). Mean
544 (red) and SEM (shading) were calculated over light stimulation trials.

545 (**A3**) Average change in GFP signal from all neurons (268 neurons) simultaneously imaged in the same site.
546 Mean (red) and SEM (shading) were calculated over light stimulation trials.

547 (**A4**) Variance in average GFP signal in this example L2/3 site in V1 explained by area of the example blood
548 vessel and by the change in GFP signal from a ROI within the blood vessel.

549 (**B**) As in **A**, from an imaging site in L5 of V1.

550 (**C**) As in **A**, from an imaging site in L2/3 of ACC on locomotion onset.

551 (**D**) Percentage of variance in neuronal GFP signal to individual events explained by the change in GFP
552 signal from blood vessel ROIs. Boxes show 25th and 75th percentile, central mark is the median, and the
553 whiskers extend to the most extreme datapoints not considered outliers.

554 (**E**) Percentage of variance in neuronal GFP signal over the entire recording explained by blood vessel GFP
555 signal per imaging location. Each datapoint is one imaging site. Boxes show 25th and 75th percentile, central
556 mark is the median, and the whiskers extend to the most extreme datapoints not considered outliers.

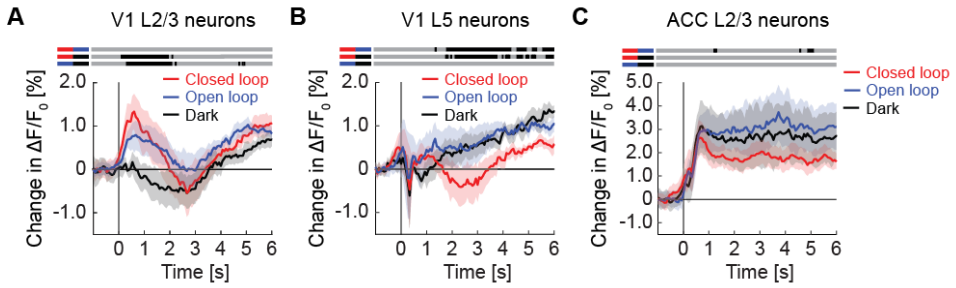

Figure 5. GFP responses at locomotion onset depended on visuomotor condition and cortical region.

(**A**) Average GFP response in L2/3 neurons in V1 on locomotion onset in closed loop (in red), in open loop (in blue), and in darkness (in grey). Here and in subsequent panels, bins with a significant difference ($p < 0.01$) are indicated by a black line above the plot (lines compared are marked on the left by pairs of colored horizontal bars); those with $p > 0.01$ are marked gray. Mean (solid lines) and the bootstrap standard error (shading) are calculated as hierarchical bootstrap estimate for each time bin.

(**B**) As in **A**, but for L5 neurons in V1.

(**C**) As in **A**, but for L2/3 neurons in ACC.

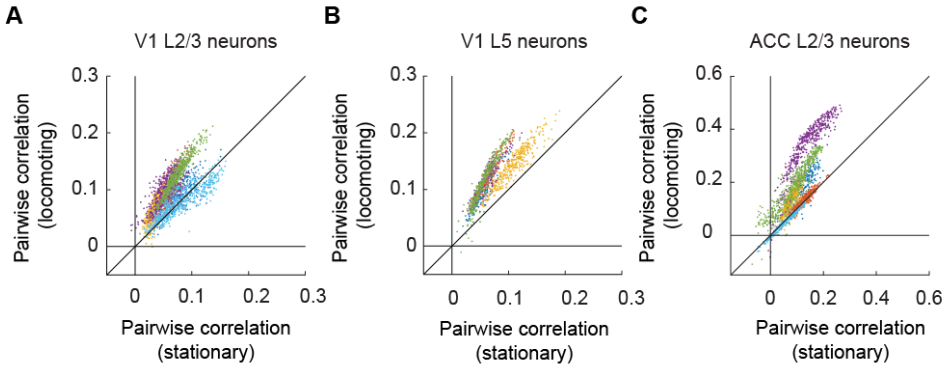

Figure 6. Locomotion increased pairwise correlation of GFP signals between neurons.

(**A**) Average pairwise correlation in GFP signal of V1 L2/3 neurons while mice were stationary and while they were locomoting. Each dot is the mean pairwise correlation of one neuron to all other neurons in the same imaging site. Colors indicate data from different mice.

(**B**) As in **A**, but for V1 L5 neurons.

(**C**) As in **A**, but for ACC L2/3 neurons.

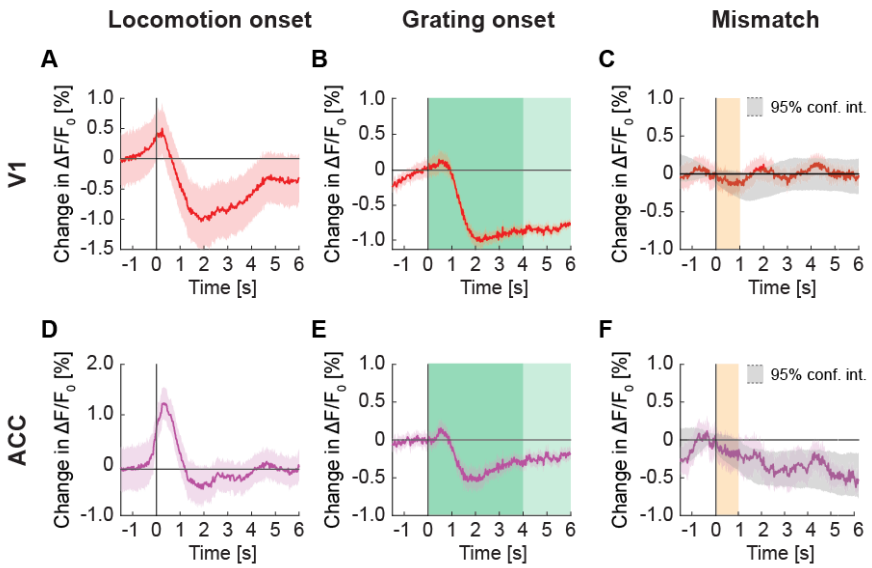

Figure 7. Signals in widefield fluorescence imaging of V1 and ACC in mice expressing GFP.

(**A**) Average change in signal from V1 on locomotion onset. Mean (solid lines) and the bootstrap standard error (shading) are calculated as hierarchical bootstrap estimate for each time bin.

(**B**) As in **A**, but for grating onset in V1. Grating duration were randomly selected between 4 s and 8 s (green shading).

(**C**) As in **A**, but on visuomotor mismatch in V1. Orange shading marks the duration of visuomotor mismatch. Gray shading marks the 95% confidence interval.

(**D**) As in **A**, but for change in signal from ACC on locomotion onset.

(**E**) As in **B**, but for change in signal from ACC on grating onset.

(**F**) As in **C**, but for change in signal from ACC on visuomotor mismatch.

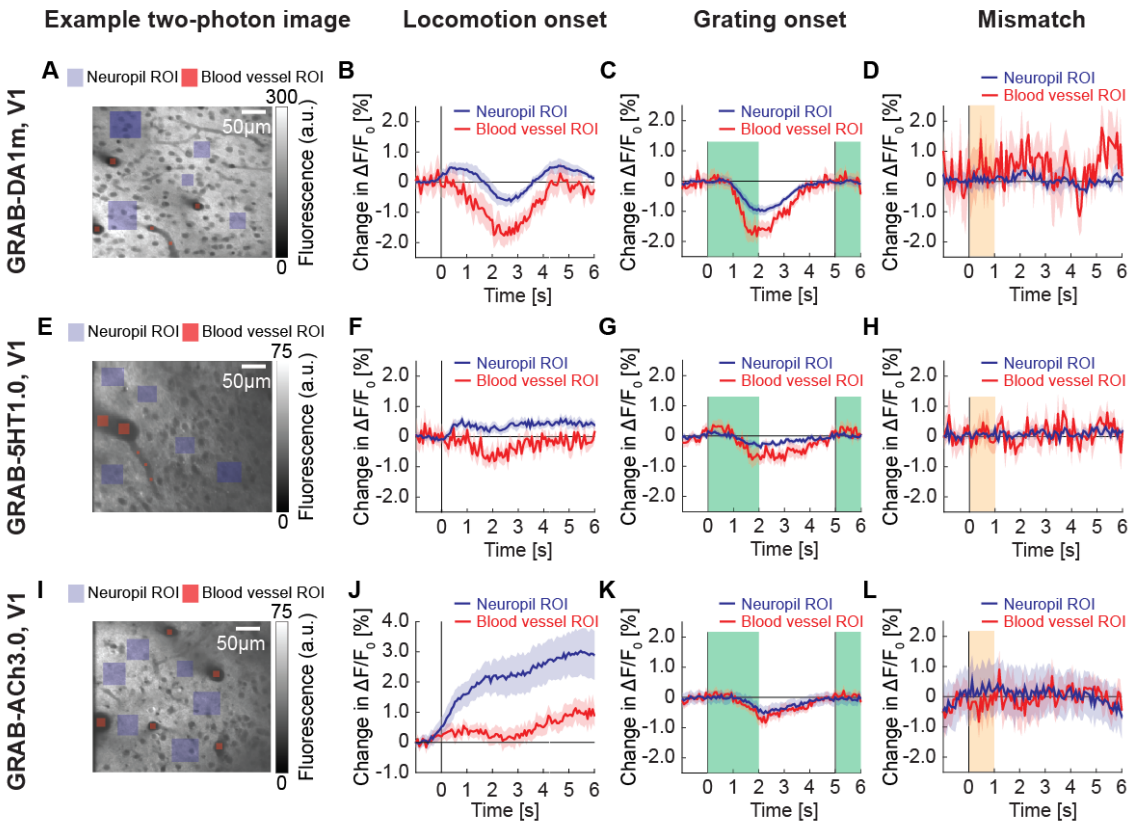

584

585 **Figure 8. GRAB signals in V1 with two-photon imaging.**

586 (**A**) Example two-photon image taken in V1 of mouse expressing GRAB-DA1m, with neuropil ROIs (in
587 violet) and blood vessel ROIs (in red).

588 (**B**) Average change in GRAB-DA1m signal in V1 on locomotion onset in ROIs over neuropil (in black) and
589 in ROIs in blood vessels (in red). Mean (solid lines) and the bootstrap standard error (shading) are
590 calculated as hierarchical bootstrap estimate for each time bin.

591 (**C**) As in **B**, but for response to grating onset. Green shading marks the duration of the gratings.

592 (**D**) As in **B**, but for response to visuomotor mismatch. Orange shading marks the duration of visuomotor
593 mismatch.

594 (**E**) Example two-photon image taken in V1 of mouse expressing GRAB-5HT1.0, with neuropil ROIs (in
595 green) and blood vessel ROIs (in red).

596 (**F**) Average change in GRAB-5HT1.0 signal in V1 on locomotion onset in ROIs over neuropils (in black) and
597 in ROIs in blood vessels (in red).

598 (**G**) As in **F**, but for response to grating onset.

599 (**H**) As in **F**, but for response to visuomotor mismatch.

600 (**I**) Example two-photon image of mouse expressing GRAB-ACh3.0 in V1, with neuropil ROIs (in green) and
601 blood vessel ROIs (in red).

602 (**J**) Average change in GRAB-ACh3.0 fluorescence in V1 in response to locomotion onset in ROIs over
603 neuropil (in black) and in ROIs over blood vessels (in red).

604 (**K**) As in **J**, but for response to grating onset.

605 (**L**) As in **J**, but for response to visuomotor mismatch.

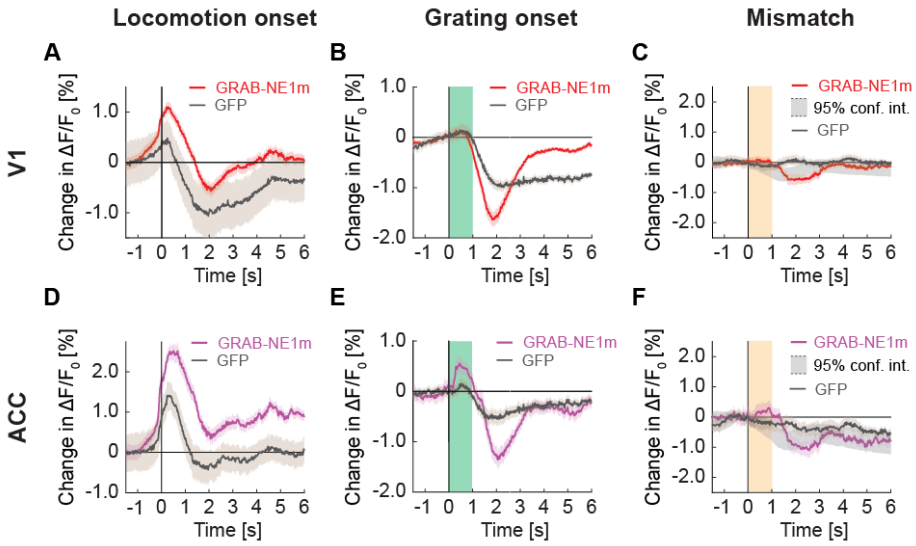

606

607 **Figure 9. Signals of V1 and ACC in widefield imaging in mice expressing GRAB-NE1m.**

608 (**A**) Average change in signal from V1 on locomotion onset. Mean (solid lines) and the bootstrap standard
609 error (shading) are calculated as hierarchical bootstrap estimate for each time bin. Here and below, GFP
610 response (in gray) from **Figure 7** overlaid.

611 (**B**) As in **A**, but for grating onset in V1. Green shading marks the duration of the gratings.

612 (**C**) As in **A**, but for visuomotor mismatch in V1. Orange shading marks the duration of visuomotor
613 mismatch. Gray shading marks the 95% confidence interval.

614 (**D**) As in **A**, but for change in signal from ACC on locomotion onset.

615 (**E**) As in **B**, but for change in signal from ACC on grating onset.

616 (**F**) As in **C**, but for change in signal from ACC on visuomotor mismatch.

617 **SUPPLEMENTARY FIGURES**

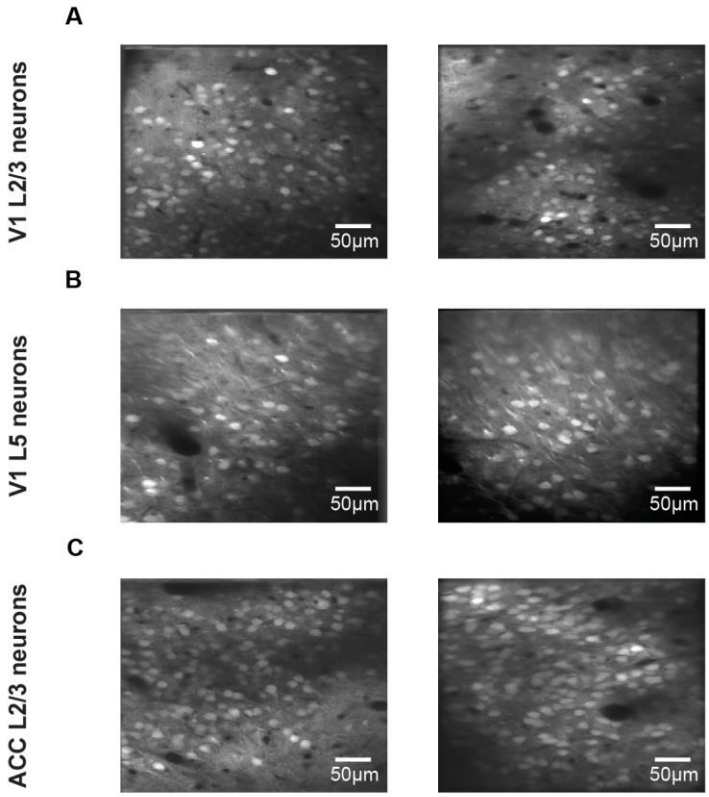

618

619 **Figure S1. Example imaging sites.**

620 (**A**) Example of two imaging sites in L2/3 of V1.

621 (**B**) Example of two imaging sites in L5 of V1.

622 (**C**) Example of two imaging sites in L2/3 of ACC.

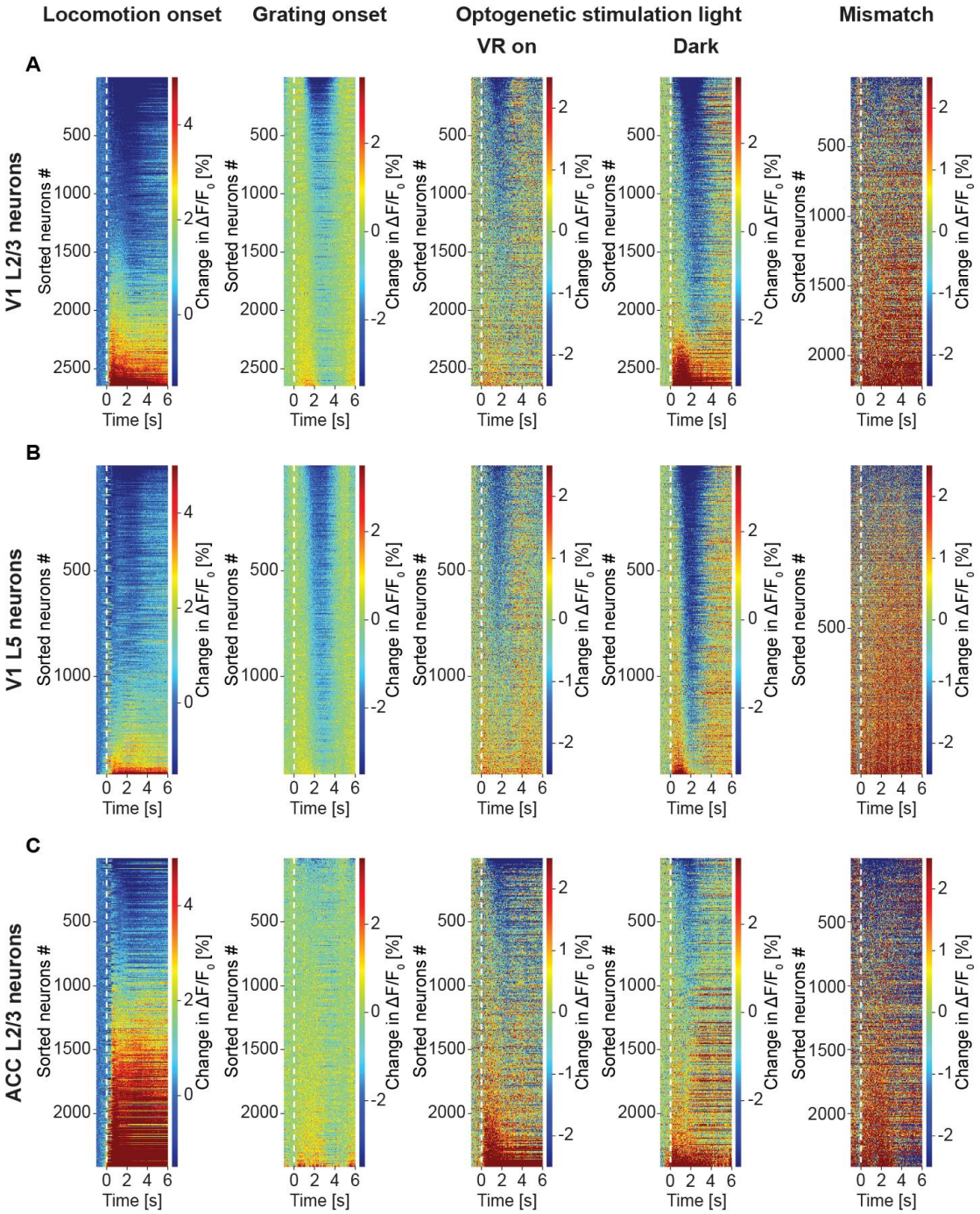

Figure S2. GFP response heatmaps. Related to Figure 1.

(**A**) Trial-averaged change in apparent GFP fluorescence in L2/3 neurons in V1 to 5 different stimuli: locomotion onset, grating onset, optogenetic light stimulation with the VR on and in dark, and visuomotor

mismatch. Note, the colormap is different for different panels and not always symmetric around 0 to illustrate all changes.

(**B**) As in **A**, but for L5 neurons in V1.

(**C**) As in **A**, but for L2/3 neurons in ACC.

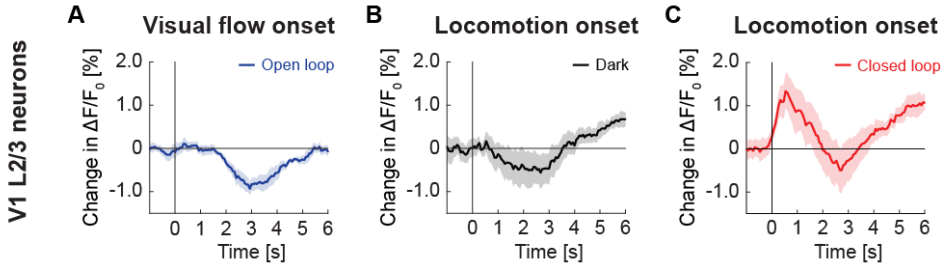

Figure S3. GFP response in V1 L2/3 on locomotion onset in closed loop was not a linear sum of component responses. Related to Figure 1.

(**A**) Average change in GFP signal from L2/3 in V1 in response to visual flow onset in open loop during stationary periods. Mean (solid lines) and the bootstrap standard error (shading) are calculated as hierarchical bootstrap estimate for each time bin.

(**B**) As in **A**, but locomotion onset in dark.

(**C**) As in **A**, but for locomotion onset in closed loop.

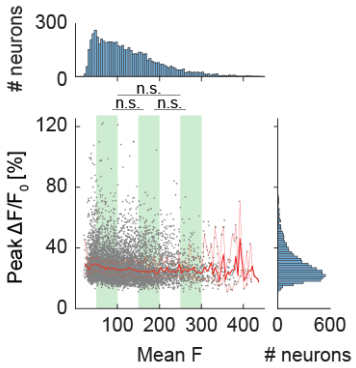

Figure S4. Peak GFP response of neurons cannot be explained by GFP expression levels. Related to Figure 3.

The peak $\Delta F/F_0$ response of each neuron is plotted against the mean GFP fluorescence intensity. Each dot is a neuron. Superimposed are the hierarchical bootstrap estimates of the median (dark red line) and 95% confidence intervals (light red lines) for each GFP fluorescence bin. We found no evidence of a difference in peak $\Delta F/F_0$ response between low, intermediate, and high GFP fluorescence expression levels (indicated by green shading) in our dataset. This is as one would expect, assuming the baseline fluorescence F_0 is above the noise floor.

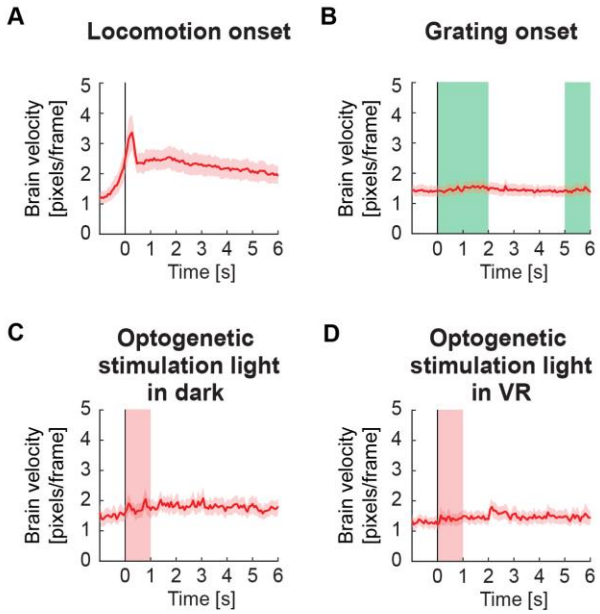

Figure S5. Brain motion estimate. Related to Figure 4.

(**A**) Estimate of average absolute brain velocity in pixels per frame at locomotion onset across all imaging sites. This estimate is based on the pixel-wise frame shift correction in the x and y directions. Note, these shifts are corrected in the data. Mean (solid lines) and the bootstrap standard error (shading) are calculated as hierarchical bootstrap estimate for each time bin. Euclidean displacement was calculated as the room-mean-squared x- and y- displacement of the imaging site.

(**B**) As in **A**, but for grating onsets. Green shading marks the duration of the gratings. There is no appreciable change in brain velocity on visual stimulation.

(**C**) As in **A**, but for optogenetic stimulation light presentation in dark. Pink shading marks the duration of the light stimulus.

(**D**) As in **A**, but for optogenetic stimulation light presentation in VR. Pink shading marks the duration of the light stimulus.

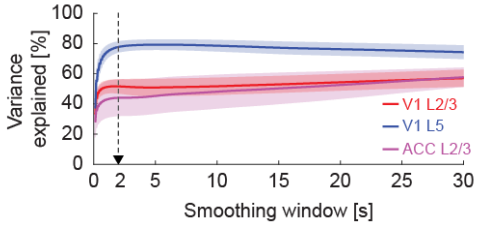

Figure S6. The variance of neuronal GFP signal explained by blood vessel GFP signal as a function of smoothing window. Related to Figure 4E.

Black arrow indicates the smoothing window used in **Figure 4E**.

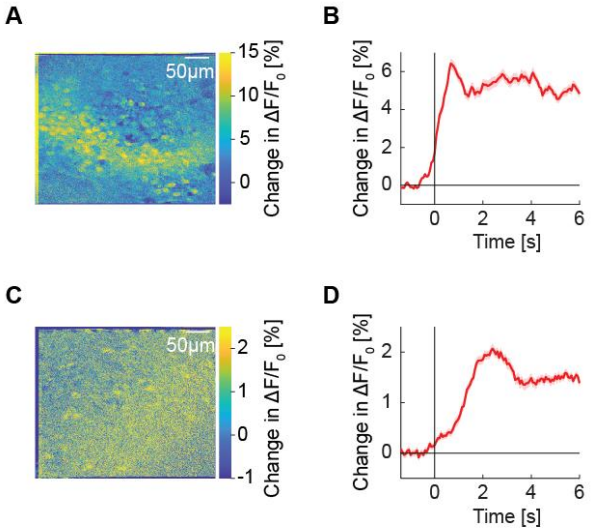

Figure S7. Average locomotion onset response during two-photon GFP imaging. Related to Figure 4.

(**A**) Putative blood vessel shadow cast on an example imaging plane on locomotion onset. Shown is the baseline subtracted average pixelwise map of GFP response on locomotion onset.

(**B**) Average GFP response of all neurons from the imaging site in **A**.

(**C**) Example of a typical response on locomotion onset. Here shadowing is likely caused by blood vessels closer to the surface of the brain.

(**D**) Average GFP response of all neurons from the imaging site in **C**.

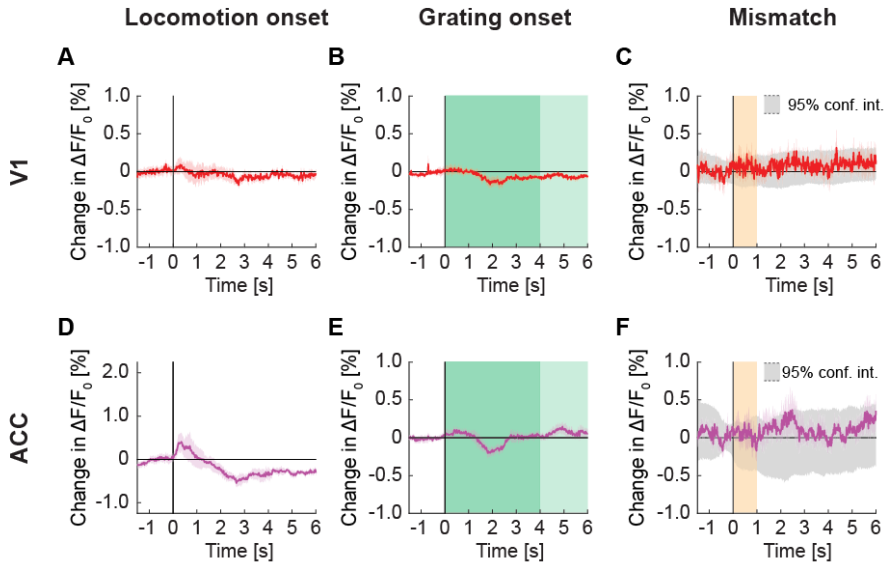

Figure S8. Signals in widefield fluorescence imaging of V1 and ACC in mice not expressing a fluorophore. Related to Figure 7.

(**A**) Average change in signal from V1 on locomotion onset. Mean (solid lines) and the bootstrap standard error (shading) are calculated as hierarchical bootstrap estimate for each time bin, in mice not expressing a fluorophore.

(**B**) As in **A**, but on grating onset in V1. Grating duration were randomly selected between 4 s and 8 s (green shading).

(**C**) As in **A**, but on visuomotor mismatch in V1. Orange shading indicates the duration of visuomotor mismatch.

(**D**) As in **A**, but for change in signal from ACC on locomotion onset.

(**E**) As in **B**, but for change in signal from ACC on grating onset.

(**F**) As in **C**, but for change in signal from ACC on visuomotor mismatch.

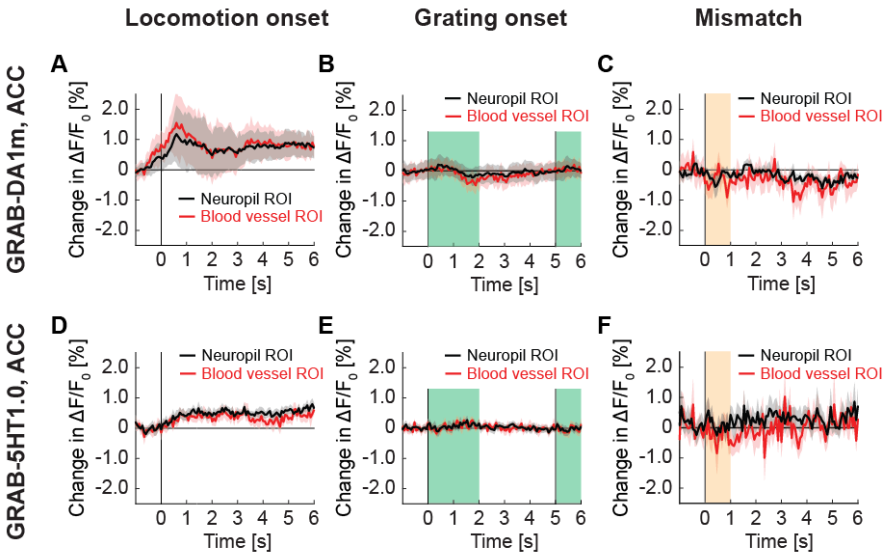

Figure S9. GRAB signals in ACC recorded with two-photon imaging. Related to Figure 8.

(**A**) Average change in GRAB-DA1m signal in ACC on locomotion onset in ROIs over neuropil (in black) and in ROIs over blood vessels (in red). Mean (solid lines) and the bootstrap standard error (shading) are calculated as hierarchical bootstrap estimate for each time bin.

(**B**) As in **A**, but for response to full-field grating onset. Green shading marks the duration of the gratings.

(**C**) As in **A**, but for response to visuomotor mismatch.

(**E**) Average change in GRAB-5HT1.0 signal in ACC on locomotion onset in ROIs over neuropil (in black) and in ROIs over blood vessels (in red).

(**F**) As in **G**, but for response to grating onset.

(**G**) As in **G**, but for response to visuomotor mismatch.

ACKNOWLEDGEMENTS

We thank all the members of the Keller lab for discussion and support. This project has received funding from the Swiss National Science Foundation (GBK), the Novartis Research Foundation (GBK), and the European Research Council (ERC) under the European Union's Horizon 2020 research and innovation programme (grant agreement No 865617) (GBK).

AUTHOR CONTRIBUTIONS

BY designed the experiments. BY performed the two-photon imaging experiments, RJ performed the widefield imaging of GRAB-NE1m experiments, and RJ and MH performed the widefield imaging of GFP and with no fluorophore experiments. BY analyzed the data. BY and GK wrote the manuscript.

DECLARATION OF INTERESTS

The authors declare no competing financial interests.

710 **REFERENCES**

711 Allen, W.E., Kauvar, I.V., Chen, M.Z., Richman, E.B., Yang, S.J., Chan, K., Gradinaru, V., Deverman, B.E.,
712 Luo, L., Deisseroth, K., 2017. Global Representations of Goal-Directed Behavior in Distinct Cell
713 Types of Mouse Neocortex. Neuron 94, 891-907.e6.
714 https://doi.org/10.1016/j.neuron.2017.04.017
715 Attinger, A., Wang, B., Keller, G.B., 2017. Visuomotor Coupling Shapes the Functional Development of
716 Mouse Visual Cortex. Cell 169, 1291-1302.e14. https://doi.org/10.1016/j.cell.2017.05.023
717 Attwell, D., Buchan, A.M., Charpak, S., Lauritzen, M., MacVicar, B.A., Newman, E.A., 2010. Glial and
718 neuronal control of brain blood flow. Nature 468, 232–243.
719 https://doi.org/10.1038/nature09613
720 Aydın, Ç., Couto, J., Giugliano, M., Farrow, K., Bonin, V., 2018. Locomotion modulates specific functional
721 cell types in the mouse visual thalamus. Nat. Commun. 9, 4882.
722 https://doi.org/10.1038/s41467-018-06780-3
723 Berger, B., Gaspar, P., Verney, C., 1991. Dopaminergic innervation of the cerebral cortex: unexpected
724 differences between rodents and primates. Trends Neurosci. 14, 21–27.
725 https://doi.org/10.1016/0166-2236(91)90179-x
726 Chen, T.-W., Wardill, T.J., Sun, Y., Pulver, S.R., Renninger, S.L., Baohan, A., Schreiter, E.R., Kerr, R.A.,
727 Orger, M.B., Jayaraman, V., Looger, L.L., Svoboda, K., Kim, D.S., 2013. Ultrasensitive fluorescent
728 proteins for imaging neuronal activity. Nature 499, 295–300.
729 https://doi.org/10.1038/nature12354
730 Chesler, M., 2003. Regulation and modulation of pH in the brain. Physiol. Rev. 83, 1183–1221.
731 https://doi.org/10.1152/physrev.00010.2003
732 Couto, J., Musall, S., Sun, X.R., Khanal, A., Gluf, S., Saxena, S., Kinsella, I., Abe, T., Cunningham, J.P.,
733 Paninski, L., Churchland, A.K., 2021. Chronic, cortex-wide imaging of specific cell populations
734 during behavior. Nat. Protoc. 16, 3241–3263. https://doi.org/10.1038/s41596-021-00527-z
735 Dadarlat, M.C., Stryker, M.P., 2017. Locomotion enhances neural encoding of visual stimuli in mouse V1.
736 J. Neurosci. 37, 3764–3775. https://doi.org/10.1523/JNEUROSCI.2728-16.2017
737 Dombeck, D.A., Khabbaz, A.N., Collman, F., Adelman, T.L., Tank, D.W., 2007. Imaging Large-Scale Neural
738 Activity with Cellular Resolution in Awake, Mobile Mice. Neuron 56, 43–57.
739 https://doi.org/10.1016/j.neuron.2007.08.003
740 Dos Santos, N.V., Saponi, C.F., Ryan, T.M., Primo, F.L., Greaves, T.L., Pereira, J.F.B., 2020. Reversible and
741 irreversible fluorescence activity of the Enhanced Green Fluorescent Protein in pH: Insights for
742 the development of pH-biosensors. Int. J. Biol. Macromol. 164, 3474–3484.
743 https://doi.org/10.1016/j.ijbiomac.2020.08.224
744 Erisken, S., Vaiceliunaite, A., Jurjut, O., Fiorini, M., Katzner, S., Busse, L., 2014. Effects of Locomotion
745 Extend throughout the Mouse Early Visual System. Curr. Biol. 24, 2899–2907.
746 https://doi.org/10.1016/j.cub.2014.10.045
747 Feng, J., Zhang, C., Lischinsky, J.E., Jing, M., Zhou, J., Wang, H., Zhang, Y., Dong, A., Wu, Z., Wu, H., Chen,
748 W., Zhang, P., Zou, J., Hires, S.A., Zhu, J.J., Cui, G., Lin, D., Du, J., Li, Y., 2019. A Genetically
749 Encoded Fluorescent Sensor for Rapid and Specific In Vivo Detection of Norepinephrine. Neuron
750 102, 745-761.e8. https://doi.org/10.1016/j.neuron.2019.02.037
751 Hamada, H.T., Abe, Y., Takata, N., Taira, M., Tanaka, K.F., Doya, K., 2023. Optogenetic activation of
752 dorsal raphe serotonin neurons induces brain-wide activation.
753 https://doi.org/10.1101/2022.08.07.503074

Iadecola, C., Nedergaard, M., 2007. Glial regulation of the cerebral microvasculature. Nat. Neurosci. 10, 1369–1376. https://doi.org/10.1038/nn2003

Jing, M., Li, Yuexuan, Zeng, J., Huang, P., Skirzewski, M., Peng, W., Qian, T., Tan, K., Wu, R., Zhang, S., Pan, S., Xu, M., Li, H., Saksida, L.M., Prado, V.F., Bussey, T., Prado, M.A.M., Cheng, H., Li, Yulong, 2019. An optimized acetylcholine sensor for monitoring in vivo cholinergic activity 1–37.

Keller, G.B., Bonhoeffer, T., Hübener, M., 2012. Sensorimotor Mismatch Signals in Primary Visual Cortex of the Behaving Mouse. Neuron 74, 809–815. https://doi.org/10.1016/j.neuron.2012.03.040

Kneen, M., Farinas, J., Li, Y., Verkman, A.S., 1998. Green fluorescent protein as a noninvasive intracellular pH indicator. Biophys. J. 74, 1591–1599. https://doi.org/10.1016/S0006-3495(98)77870-1

Leinweber, M., Ward, D.R., Sobczak, J.M., Attinger, A., Keller, G.B., 2017. A Sensorimotor Circuit in Mouse Cortex for Visual Flow Predictions. Neuron 95, 1420-1432.e5. https://doi.org/10.1016/j.neuron.2017.08.036

Leinweber, M., Zmarz, P., Buchmann, P., Argast, P., Hübener, M., Bonhoeffer, T., Keller, G.B., 2014. Two-photon Calcium Imaging in Mice Navigating a Virtual Reality Environment. J. Vis. Exp. 1–6. https://doi.org/10.3791/50885

Lohani, S., Moberly, A.H., Benisty, H., Landa, B., Jing, M., Li, Y., Higley, M.J., Cardin, J.A., 2022. Spatiotemporally heterogeneous coordination of cholinergic and neocortical activity. Nat. Neurosci. 25, 1706–1713. https://doi.org/10.1038/s41593-022-01202-6

Ma, Y., Shaik, M.A., Kim, S.H., Kozberg, M.G., Thibodeaux, D.N., Zhao, H.T., Yu, H., Hillman, E.M.C., 2016. Wide-field optical mapping of neural activity and brain haemodynamics: considerations and novel approaches. Philos. Trans. R. Soc. B Biol. Sci. 371, 20150360. https://doi.org/10.1098/rstb.2015.0360

Mächler, P., Fomin-Thunemann, N., Thunemann, M., Sætra, M.J., Desjardins, M., Kılıç, K., Şencan, I., Li, B., Saisan, P., Cheng, Q., Weldy, K.L., Boas, D.A., Buxton, R.B., Einevoll, G.T., Dale, A.M., Sakadžić, S., Devor, A., 2021. Microscopic Quantification of Oxygen Consumption across Cortical Layers. https://doi.org/10.1101/2021.10.13.464176

Ocana-Santero, G., Packer, A.M., Sharp, T., Butt, S.J.B., 2024. In Vivo Two-Photon Microscopy Reveals Sensory-Evoked Serotonin (5-HT) Release in Adult Mammalian Neocortex. ACS Chem. Neurosci. 15, 456–461. https://doi.org/10.1021/acschemneuro.3c00725

Raimondo, J.V., Joyce, B., Kay, L., Schlagheck, T., Newey, S.E., Srinivas, S., Akerman, C.J., 2013. A genetically-encoded chloride and pH sensor for dissociating ion dynamics in the nervous system. Front. Cell. Neurosci. 7, 202. https://doi.org/10.3389/fncel.2013.00202

Ruff, C.F., Anaya, F.J., Dienel, S.J., Rakymzhan, A., Altamirano-Espinoza, A., Couey, J.J., Fukuda, M., Watson, A.M., Su, A., Fish, K.N., Rubio, M.E., Hooks, B.M., Ross, S.E., Vazquez, A.L., 2024. Long-range inhibitory neurons mediate cortical neurovascular coupling. Cell Rep. 43. https://doi.org/10.1016/j.celrep.2024.113970

Saravanan, V., Berman, G.J., Sober, S.J., 2020. Application of the hierarchical bootstrap to multi-level data in neuroscience. Neurons Behav. Data Anal. Theory 3, https://nbdt.scholasticahq.com/article/13927-application-of-the-hierarchical-bootstrap-to-multi-level-data-in-neuroscience.

Scott, B.B., Thiberge, S.Y., Guo, C., Tervo, D.G.R., Brody, C.D., Karpova, A.Y., Tank, D.W., 2018. Imaging cortical dynamics in GCaMP transgenic rats with a head-mounted widefield macroscope. Neuron 100, 1045-1058.e5. https://doi.org/10.1016/j.neuron.2018.09.050

Shen, Z., Lu, Z., Chhatbar, P.Y., O'Herron, P., Kara, P., 2012. An artery-specific fluorescent dye for studying neurovascular coupling. Nat. Methods 9, 273–276. https://doi.org/10.1038/nmeth.1857

Sun, F., Zeng, J., Jing, M., Zhou, J., Feng, J., Owen, S.F., Luo, Y., Li, F., Wang, H., Yamaguchi, T., Yong, Z., Gao, Y., Peng, W., Wang, L., Zhang, S., Du, J., Lin, D., Xu, M., Kreitzer, A.C., Cui, G., Li, Y., 2018. A Genetically Encoded Fluorescent Sensor Enables Rapid and Specific Detection of Dopamine in Flies, Fish, and Mice. Cell 174, 481-496.e19. https://doi.org/10.1016/j.cell.2018.06.042

Valley, M.T., Moore, M.G., Zhuang, J., Mesa, N., Castelli, D., Sullivan, D., Reimers, M., Waters, J., 2020. Separation of hemodynamic signals from GCaMP fluorescence measured with wide-field imaging. J. Neurophysiol. 123, 356–366. https://doi.org/10.1152/jn.00304.2019

Wan, J., Peng, W., Li, X., Qian, T., Song, K., Zeng, J., Deng, F., Hao, S., Feng, J., Zhang, P., Zhang, Y., Zou, J., Pan, S., Shin, M., Venton, B.J., Zhu, J.J., Jing, M., Xu, M., Li, Y., 2021. A genetically encoded sensor for measuring serotonin dynamics. Nat. Neurosci. 24, 746–752. https://doi.org/10.1038/s41593-021-00823-7

Waters, J., 2020. Sources of widefield fluorescence from the brain. eLife 9, 1–13. https://doi.org/10.7554/eLife.59841

Widmer, F.C., O'Toole, S.M., Keller, G.B., 2022. NMDA receptors in visual cortex are necessary for normal visuomotor integration and skill learning. eLife 11, e71476. https://doi.org/10.7554/eLife.71476

Yogesh, B., Keller, G.B., 2023. Cholinergic input to mouse visual cortex signals a movement state and acutely enhances layer 5 responsiveness. eLife 12. https://doi.org/10.7554/eLife.89986

Zhang, W.-T., Chao, T.-H.H., Yang, Y., Wang, T.-W., Lee, S.-H., Oyarzabal, E.A., Zhou, J., Nonneman, R., Pegard, N.C., Zhu, H., Cui, G., Shih, Y.-Y.I., 2022. Spectral fiber photometry derives hemoglobin concentration changes for accurate measurement of fluorescent sensor activity. Cell Rep. Methods 2, 100243. https://doi.org/10.1016/j.crmeth.2022.100243

Zmarz, P., Keller, G.B., 2016. Mismatch Receptive Fields in Mouse Visual Cortex. Neuron 92, 766–772. https://doi.org/10.1016/j.neuron.2016.09.057